8. [η] of PFA possibly as well as PMA increases with α at lower α, attains a maximum near $\alpha = 0.5$ and then decreases beyond it, and finally the solution becomes turbid.

Acknowledgment. We are greatly indebted to Dr. Miyazaki and Dr. Kato of Nagoya University for the radiation polymerization of maleic anhydride. We also thank Prof. Nagasawa of Toyota Technological Institute for the helpful discussion on the model calculation.

References and Notes

(1) Rice, S. A.; Nagasawa, M. *Polyelectrolyte Solutions*; Academic: New York, 1961.
(2) Selegny, E., Ed. *Polyelectrolytes*; D. Reidel: Amsterdam, 1972.
(3) Kotin, L.; Nagasawa, M. *J. Chem. Phys.* **1962**, *36*, 873.
(4) Sugai, S.; Nitta, K. *Biopolymers* **1973**, *12*, 1363.
(5) Manning, G. S. *J. Chem. Phys.* **1969**, *51*, 924.
(6) Nagasawa, M.; Murase, T.; Kondo, K. *J. Phys. Chem.* **1965**, *69*, 4005.
(7) Kawaguchi, Y.; Nagasawa, M. *J. Phys. Chem.* **1969**, *73*, 4382.
(8) Kitano, T.; Fujimoto, T.; Nagasawa, M. *Polym. J. (Tokyo)* **1977**, *9*, 153.
(9) Inagaki, H.; Yukioka, S.; Hayakawa, M.; Noda, I.; Nagasawa, M.; Kitano, T. *Polym. Prepr. Jpn.* **1985**, *34*, 2701.
(10) Kitano, T.; Taguchi, A.; Noda, I.; Nagasawa, M. *Macromolecules* **1980**, *13*, 537.
(11) Nagasawa, M.; Kitano, T.; Noda, I. *Biophys. Chem.* **1980**, *11*, 435.
(12) Lang, J. L.; Pavelich, W. A.; Clarey, H. D. *J. Polym. Sci., Part A* **1963**, *A1*, 1123.
(13) Sakurada, I.; Sakaguchi, Y.; Horin, S.; Uehara, H. *Kobunshi Kagaku*, **1970**, *27*, 74.
(14) Muto, N.; Kamatsu, T.; Nakagawa, T. *Bull. Chem. Soc. Jpn.* **1973**, *46*, 2711.
(15) Barone, G.; Rizzo, E. *Gaz. Chim. Ital.* **1973**, *103*, 401.
(16) Ferry, J. D.; Udy, D. G.; Wu, F. G.; Hechkler, G. E.; Fordyce, D. B. *J. Colloid Sci.* **1951**, *6*, 429.
(17) Dubin, P. L.; Strauss, U. P. *J. Phys. Chem.* **1967**, *71*, 2757 and their subsequent papers.
(18) Ohno, N.; Nitta, K.; Makino, S.; Sugai, S. *J. Polym. Sci., Polym. Phys. Ed.* **1973**, *11*, 413 and their subsequent papers.
(19) Otsu, T.; Yasuhara, Y.; Shiraishi, K.; Mori, S. *Polym. Bull. (Berlin)* **1984**, *12*, 449 and their subsequent papers.
(20) Kitano, T.; Ishigaki, A.; Uematsu, G.; Kawaguchi, S.; Ito. K. *J. Polym. Sci., Polym. Chem. Ed. 1987*, 25, 979.
(21) Kitano, T.; Kawaguchi, S.; Minakata, A., in preparation.
(22) Gregor, H. P.; Frederick, M. *J. Polym. Sci.* **1957**, *23*, 451.
(23) Flory, P. J. *Principles of Polymer Chemistry*; Cornell University Press: Ithaca, NY, 1955.
(24) Kortüm, G.; Vogel, W.; Andrussov, K., Ed. *Dissociation Constants of Organic Acids in Aqueous Solution*; Butterworths: London, 1961.
(25) Laskowski, M.; Scheraga, H. A. *J. Am. Chem. Soc.* **1954**, *76*, 6305.
(26) Leyte, J. C.; Zuiderweg, L. H.; Vledder, H. J. *Spectrochim. Acta, Part A* **1967**, *23*, 1397.
(27) Nagasawa, M.; Holtzer, A. *J. Am. Chem. Soc.* **1964**, *86*, 531.
(28) Dubin, P. L.; Strauss, U. P. *J. Phys. Chem.* **1970**, *74*, 2842.
(29) Schultz, A. W.; Strauss, U. P. *J. Phys. Chem.* **1972**, *76*, 1767.
(30) Ohno, N.; Sugai, S. *Macromolecules* **1985**, *18*, 1291.
(31) Muroga, Y.; Noda, I.; Nagasawa, M. *Macromolecules* **1985**, *18*, 1576.
(32) Takahashi, A.; Nagasawa, M. *J. Am. Chem. Soc.* **1964**, *86*, 543.
(33) Noda, I.; Tsuge, T.; Nagasawa, M. *J. Phys. Chem.* **1970**, *74*, 710.
(34) Leyte, J. C.; Mandel, M. *J. Polym. Sci., Part* A-2 **1964**, *A2*, 1879.

Polymer Probe Dynamics

Benjamin Chu* and Dan-qing Wu

Chemistry Department, State University of New York at Stony Brook, Long Island, New York 11794-3400. *Received September 17, 1986*

ABSTRACT: A quaternary polymer solution system consisting of polystyrene (PS), poly(methyl methacrylate) (PMMA), toluene (TOL), and α-chloronaphthalene (CNA) has been selected to study the structure (size) and dynamics [translational (and internal) motions] of both the polymer pseudonetwork and the probe. In this work, a trace amount of poly(methyl methacrylate) with $M_w = 5.7 \times 10^6$ and $M_w/M_n \sim 1.2$ was used as the "optically labeled" chain (probe) diffusing in the polystyrene ($M_w = 2.0 \times 10^7$, $M_w/M_n \sim 1.8$) pseudonetwork. The pseudonetwork was formed by dissolving PS in an isorefractive mixed solvent (MS) of TOL and CNA. At 38 °C and with a volume fraction $\phi_{CNA} = 0.72$ in the mixed solvent, PS (with preferential adsorption) was refractive index matched. The absolute scattered intensity of the refractive index matched polymer solution (PS/MS) was comparable to the scattering power of the mixed solvent. Static and dynamic light scattering measurements were used to characterize the probe (PMMA) and the polymer (PS) pseudonetwork separately. By changing the MS composition, we could characterize the structure and the dynamics of PS in the mixed solvent in semidilute solutions. Thus, we were able to determine independently static and dynamic properties of the polymer matrix, such as the correlation length (L, or mesh size) and the cooperative diffusion coefficient (D_c). Properties of the isorefractive polymer (PS) matrix were obtained by interpolation. The structure (size), dynamics, and interaction of the PMMA probe could then be investigated in detail in the well-characterized PS/MS isorefractive matrix. In particular, photocount autocorrelation function measurements of the PMMA probe in the PS/MS matrix showed the presence of at least two dominant characteristic modes even at small scattering angles for R_g(PMMA) $\gg L$(PS). The slow mode could be identified with the translational motion of the center of mass of the PMMA probe chain while we suggest that the fast mode might be related to a coupling of PMMA motions with the cooperative motion of the PS/MS matrix.

I. Introduction

Entanglement of polymer coils in semidilute solutions is responsible for the pseudogel behavior. Dynamic light scattering of semidilute polymer solutions has shown the existence of a fast relaxation mode expressed in terms of the so-called cooperative diffusion coefficient.[1] Although observation of a very slow mode has been reported by several groups,[2] its nature remains unclear.[3-5] The very slow mode (denoted $D_{V\text{-slow}}$) was interpreted as the self-diffusion of a single polymer chain reptating through the entangled polymer coils.[2] However, the magnitude of $D_{V\text{-slow}}$ appeared to be too small when compared with the self-diffusion coefficient (D_s) obtained by other techniques such as forced Rayleigh scattering.[6] A clustering of polymer chains (rather than a single polymer chain) diffusing through the entangled polymer coils was then proposed

0024-9297/87/2220-1606$01.50/0

to explain the much smaller magnitude of $D_{V\text{-}slow}$.[7,8] There was, however, no additional independent experimental evidence to confirm this supposition. It should also be noted that $D_{V\text{-}slow}$ is not the usual slow mode that could be related to the translational motion of center of mass of the polymer coils even near the overlap concentrations.[1]

Probe diffusion measurements by light scattering have been reported.[9-13] A trace amount of polymer coils in solution or colloidal particles in suspension played the role of a single "optically labeled" probe (to be denoted by subscript P2) moving in the index-matched semidilute polymer (to be denoted by subscript P1) solution. The technique mimics the hydrogen/deuterium labeling of polymer chains in neutron scattering studies. Compatible polymer pairs such as polystyrene (PS)/PVME (poly(vinyl methyl ether) in toluene (TOL)[11] or in *o*-fluorotoluene[10] have been reported. Martin[11] showed that the scaling law for the molecular weight dependence of D_s was valid but that for the concentration dependence did not hold. The magnitude of D_s for PS in PVME/*o*-fluoroTOL was compared with the PS/CCl_4 data by pulsed-field gradient NMR and the PS/benzene data by forced Rayleigh scattering. The experimental values for D_s by the three techniques agreed qualitatively.[10] Incompatible polymer pairs should yield similar results, especially if we were to use high molecular weight polymers with low overlapping concentrations (C^*) to form the polymer matrix. Then, polymer entanglement could occur at fairly low concentrations (C), with C still satisfying the criterion $C > C^*$. Under such conditions, the probe polymer molecule is essentially surrounded by small solvent molecules. Nevertheless, it is important to realize that phase separation could occur for the polymer probe even at fairly low concentrations because of the presence of relatively large amounts of the "matrix" polymer (P1; in our case, PS) which is incompatible with the probe polymer (P2; in our case, poly(methyl methacrylate) (PMMA)).

The translational diffusion of polymers in dilute solutions of small solvent molecules follows the Stokes–Einstein relation

$$D_T = k_B T/(6\eta_0 \pi R_h) \tag{1}$$

where k_B, T, η_0, and R_h are the Boltzmann constant, the absolute temperature, the solvent viscosity, and the hydrodynamic radius, respectively. Deviations from eq 1 were observed for carboxylate-modified polystyrene latex spheres in high molecular weight polymer solutions.[13] Dynamical crossover from the Stokes–Einstein diffusion to reptation[11] and universal scaling for self-diffusion by macromolecules in solution[14] have been reported.

We have selected a quaternary system with PMMA (probe) moving in semidilute isorefractive PS (matrix) solutions of mixed solvent as our model. The quaternary system permits us to investigate the structure and dynamics of the matrix and of the probe separately. We used the PS/BZ (benzene) data[22] to estimate our C_{PS}^* value, where C^* was defined by

$$C^* = M_w/(N_A R_g^3) \tag{2}$$

and obtained $C^* = 1 \times 10^{-3}$ g/mL for PS ($M_w = 2 \times 10^7$) in benzene. We used $C^* \sim 1 \times 10^{-3}$ g/mL for PS in the mixed solvent at 38 °C since the exact value of C^* is not crucial in our discussions. Most experiments were performed with $C_{PMMA} \sim 1.2 \times 10^{-4}$ g/mL, which was roughly 40 times lower than C^* of PMMA. The presence of PMMA could also change the C^* value for PS since the solvent quality changes according to the relative amounts of PS and PMMA. The infinite dilute solution condition for the PMMA probe could be extrapolated from results at different PMMA concentrations in the dilute solution regime (for PMMA) at each fixed PS matrix concentration.

The light scattering technique is discussed briefly in section II, experimental methods are presented in section III, results and discussions are given in section IV, including a schematic physical presentation of semidilute polymer solutions that tries to account for the static and dynamic properties of polymers in semidilute regimes, and finally, the conclusion is presented in section V. We have paid particular attention to experimental details and data analysis because of the complex nature of the structure and dynamics of polymer semidilute solutions. However, we do not believe that the use of the quaternary polymer solution has added much additional complication. Instead, it permits us to have a closer examination of the interrelations between each polymer coil and the neighboring polymer matrix.

II. Light Scattering Technique

Static Light Scattering. The excess Rayleigh ratio $R_{vv}(K,C)$ of vertically polarized incident and scattered light from a dilute polymer solution can be expressed in the following general form:

$$HC/R_{vv}(K,C) = (1/M_w)P^{-1}(K) + 2A_2C + 3A_3C^2 + \ldots \tag{3}$$

where $H = 4\pi^2(dn/dC)^2 n^2/\lambda_0^4$ with n, λ_0, dn/dC, C, and N_A being the refractive index, the wavelength of light in vacuo, the refractive index increment, the polymer concentration, and Avogadro's number, respectively. K [$\equiv (4\pi n/\lambda_0) \sin(\theta/2)$] is the scattering vector, M_w is the weight-average molecular weight of the polymer. A_2 and A_3 are the second and third virial coefficients, and $P(K)$ is the single particle scattering factor due to intramolecular interference which can be expressed by

$$P^{-1}(K) = 1 + K^2 R_g^2/3 + \ldots \tag{4}$$

with R_g being the root-mean-square z-average radius of gyration of the polymer molecules in solution.

For $KR_g \lesssim 1$, and at fairly dilute concentrations, eq 3 becomes

$$HC/R_{vv}(K) = (1/M_w)(1 + K^2 R_g^2/3) + 2A_2C \tag{5}$$

M_w, R_g (at infinite dilution), and A_2 could be determined from the angular distribution of absolute light scattering intensity measurements at different concentrations based on eq 5.

In a mixed solvent (cosolvent) instead of a single solvent, preferential adsorption (or desorption) has to be taken into account unless the two solvents have identical solubility for the polymer. The preferential adsorption coefficient (α_a) is related to the refractive index increments[15]

$$\left(\frac{dn}{dC}\right)_0 = \left(\frac{dn}{dC}\right)_\phi + \alpha_a \frac{dn}{d\phi} \tag{6}$$

where $(dn/dC)_0$ is the refractive index increment at constant chemical potentials, $(dn/dC)_\phi$ is the measured refractive index increment at constant solvent composition, and ϕ is the volume fraction of solvent 1. $dn/d\phi$ can be either measured or calculated.

In the presence of preferential adsorption, light scattering intensity measurements yield mainly apparent molecular parameters ($M_{w,app}$ and $A_{2,app}$). Conversely, if we know the true polymer molecular weight, we can determine α_a. Equations 7 and 8 show the essential relationships between true and apparent properties, assuming that R_g remains unchanged

$$M_w(dn/dC)_0^2 = M_w[(dn/dC)_\phi + \alpha_a dn/d\phi]^2 = M_{w,app}(dn/dC)_\phi^2 \quad (7)$$

$$A_2 M_w = A_{2,app} M_{w,app} \quad (8)$$

In semidilute or concentrated solution regimes, eq 3 does not hold. Instead we have

$$\lim_{K\to 0} \frac{HC}{R_{vv}(K)} = (\partial\pi/\partial C)_{P,T}/RT \quad (9)$$

where R is the universal gas constant and $[C(\partial\pi/\partial C)_{P,T}]^{-1}$ is the osmotic compressibility. Log–log plots of M/RT-$(\partial\pi/\partial C)_{T,P}$ vs. C/C^* for many polymers of similar structure in solvents of comparable solvent quality have been reported to show a universal behavior.[16]

At finite concentrations in semidilute solutions, the angular distribution of the absolute scattered intensity can be represented by

$$1/R_{vv}(K) = [1/R_{vv}(0)](1 + K^2L^2/3) \quad (10)$$

where $R_{vv}(0)$ has been defined by eq 9 and L is an *average* correlation length. We have italicized average to emphasize not only the time-averaged behavior of the correlation (or screening) length but also the sources of the interference effect as measured by time-averaged light scattering intensity measurements. If we were to consider L to be due to only the characteristic length between entanglement points, then the limiting behavior for L has the form

$$L = aC^{-q} \quad (11)$$

where **a** is a constant for a given solvent and the exponent $q = \nu/(\nu d - 1)$. If d (dimensionality) = 3, $q = {}^3/_4$ for $\nu = {}^3/_5$ in a good solvent and $q = 1$ for $\nu = {}^1/_2$ in a Θ solvent.[17] Experimentally, $q < {}^3/_4$ in the literature.

When the probe polymer (P2) is dissolved in an isorefractive polymer (P1)/mixed solvent (MS) solution, static light scattering data can be analyzed in a similar manner as polymer in a mixed solvent. Again, the refractive index increment should be measured by taking the polymer (P1)/MS solution as the new solvent system. Extrapolation to infinite dilution for the probe polymer (P2) can be achieved by changing the concentration of polymer P2 at constant composition of the solvent system which changes with each concentration of the isorefractive polymer (P1) [and the probe polymer (P2)]. At the same time, we should be aware of the effects of preferential adsorption (or desorption) in a multicomponent solvent system.

Dynamic Light Scattering. In the self-beating mode, the autocorrelator measures the intensity–intensity correlation function $G^{(2)}(t)$

$$G^{(2)}(t) = A(1 + b|g^{(1)}(t)|^2) \quad (12)$$

where A is the background (or the base line), b is a spatial coherence factor and accounts for the nonideal point detector, and $|g^{(1)}(t)|$ is the normalized electric field autocorrelation function. For polydisperse polymer molecules

$$|g^{(1)}(t)| = \int_0^\infty G(\Gamma) \exp(-\Gamma t)\, d\Gamma \quad (13)$$

where Γ is a characteristic line width and $G(\Gamma)$ is the normalized characteristic line width distribution. For monodisperse, structureless particles, $\Gamma = D_T K^2$, with D_T being the translational diffusion coefficient. In discrete form, eq 13 can be written as

$$|g^{(1)}(K,t)| = \sum_i a_i(K) \exp(-\Gamma_i(K)t) \quad (14)$$

where the weighting factor $a_i(K)$ is proportional to the time-averaged intensity scattered by polymer i at scattering vector K. At infinite dilution and $KR_g \ll 1$; $a_i \sim M_i^2$.

In principle, $G(\Gamma)$ can be retrieved from $|g^{(1)}(t)|$ by Laplace inversion of eq 13. In practice, as $|g^{(1)}(t)|$ contains noise and is bandwidth limited, the Laplace inversion becomes a very difficult ill-conditioned problem. Several methods have been developed for an appropriate inversion of eq 13.[18–20]

The cumulants expansion[20] (CUMFIT) is a simple but effective procedure to determine the average line width and the width of the $G(\Gamma)$ distribution

$$|g^{(1)}(t)| = \exp[-\bar{\Gamma}t + (\mu_2/2)t^2 - (\mu_3/3!)t^3 + ...] \quad (15)$$

where the i-th cumulants μ_i has the form

$$\mu_i = d^{(i)} \ln |g^{(1)}(t)|/dt^{(i)} \quad (16)$$

with $\mu_2 = \langle(\Gamma - \bar{\Gamma})^2\rangle$ and the variance is identified by $\mu_2/\bar{\Gamma}^2$. However, this procedure is difficult to implement for broad or multimodal line-width distributions.

The double-exponential (DEXP) approach assumes that $G(\Gamma)$ is a weighted sum of two Dirac delta functions

$$G(\Gamma) = \mathbf{A}_1\delta(\Gamma - \Gamma_1) + \mathbf{A}_2\delta(\Gamma - \Gamma_2) \quad (17)$$

which corresponds to

$$|g^{(1)}(t)| = \mathbf{A}_1 \exp(-\Gamma_1 t) + \mathbf{A}_2 \exp(-\Gamma_2 t) \quad (18)$$

where $\mathbf{A}_1$ and $\mathbf{A}_2$ are proportional to the scattered intensity with characteristic line widths Γ_1 and Γ_2, respectively. $\mathbf{A}_1 + \mathbf{A}_2 = 1$.

DEXP approximates the $G(\Gamma)$ distribution function consisting of two narrow peaks. For $G(\Gamma)$ having a broad and a narrow Γ-distribution, a combination of CUMFIT and DEXP could be used

$$|g^{(1)}(t)| = \mathbf{A}_1 \exp(-\bar{\Gamma}_1 t + (\mu_{21}/2)t^2) + \mathbf{A}_2 \exp(-\Gamma_2 t) \quad (19)$$

It is important to emphasize here that although photon correlation spectroscopy can provide the most precise measured intensity–intensity time correlation function, Laplace inversion of $|g^{(1)}(t)|$ has limited resolution. For polydisperse polymer coils with internal modes in the dilute solution regime, we can determine translational motion of the polymer in terms of a translational diffusion coefficient and some information on its internal modes by means of a K^2 expression of $\bar{\Gamma}$[25]

$$\bar{\Gamma}(K) \cong \bar{D}_T^0(1 + k_d C)K^2(1 + fR_g^2K^2 + ...) \quad (20)$$

where $\bar{D}_T^0$ is the z-average translational diffusion coefficient at infinite dilution, k_d is the diffusion second virial coefficient and depends on solvent quality as well as molecular weights, and f is a dimensionless number that depends on chain structure, polydispersity, and solvent quality. All motions other than translational diffusion are partially taken into account in the K^4 term.

In the absence of a polymer network, the polydisperse probe polymer at infinite dilution obeys the Stokes–Einstein equation

$$\langle R_h^{-1}\rangle_z^{-1} = k_B T/[6\pi\eta_0 \bar{D}_T^0] \quad (21)$$

which reduces to eq 1 for independent, monodisperse, structureless particles.

III. Experimental Methods

Materials. α-Chloronaphthalene (CNA) and toluene were purchased from Aldrich Chemical Co. CNA was doubly distilled at 0.1 Torr under N_2 atmosphere. The distilled CNA was colorless. TOL was also distilled. Polystyrene ($M_w = 2 \times 10^7$, $M_w/M_n \sim 1.8$, purchased from Pressure Chemical Co.) was used without further purification.

Poly(methyl methacrylate) was kindly provided by W. Shuely (CRDC, Aberdeen Proving Ground, MD). Fractionation of the

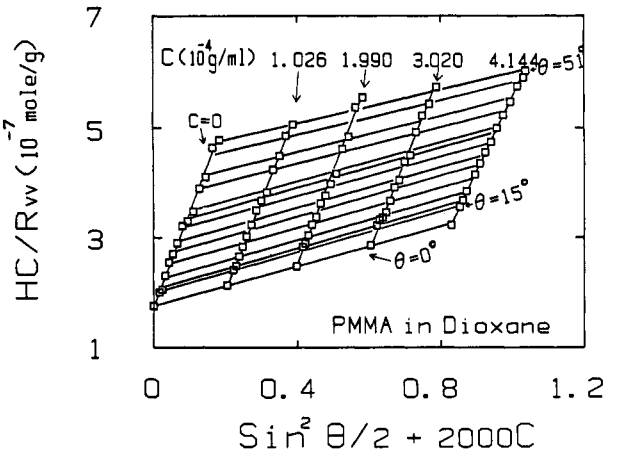

Figure 1. Zimm plot of PMMA (probe) in dioxane at 30 °C. $M_w = 5.69 \times 10^6$, $R_g = 145$ nm, and $A_2 = 1.82 \times 10^{-4}$ mol cm^3/g^2.

Table I
Refractive Index (n), Density (d), and Viscosity (η) of Solvents and Polymers at 38 °C

	CNA	TOL	MS (ϕ_{CNA} = 0.72)[a]	MS (ϕ_{CNA} = 0.45)[a]	PMMA	PS
n (λ_0 = 488 nm)	1.643	1.498	1.601	1.561	1.50	1.601
d, g/mL	1.179	0.8506	1.091	1.002	1.12	1.18
η, cP	2.94	0.413	1.34	0.867		

[a] ϕ_{CNA} is the volume fraction of CNA.

high molecular weight PMMA was carried out by methyl ethyl ketone (solvent) and methanol (precipitant). One PMMA fraction that was characterized in dioxane (a good solvent) was used for the present study. Zimm plot results yielded $M_w = 5.69 \times 10^6$, $A_2 = 1.8 \times 10^{-4}$ mol cm^3/g^2, and $R_g = 145$ nm, as shown in Figure 1. Photon correlation function measurements yielded $M_w/M_n < 1.2$.

Sample Preparation. Mixed solvents (MS) with varying compositions of CNA were prepared by weighing CNA and TOL on an analytical balance (0.1-mg resolution) and subsequent thorough mixing of the stock solvent mixtures.

Solutions of PMMA in MS or pure solvent were prepared by filtering the solution through a 0.5-μm Millipore FG filter to dust-free light scattering cells.

PS ($M_w \sim 2 \times 10^7$) solutions could not be filtered without fear of shear degradation. Thus, semidilute PS solutions with (or without) PMMA probes were prepared by filtering known concentrations of PMMA/MS solutions (or MS solvent mixtures) to known amounts of PS in dust-free volumetric flasks. It took about 1 week to dissolve PS with constant but gentle mixing. The PMMA (PS/MS) solutions were then transferred to (covered) dust-free centrifuge tubes and centrifuged for about 15 h before we transferred the solutions to dust-free light-scattering cells for experiments. Centrifuge accelerations of 700g and 3000g were used, respectively, for PS in TOL and PS in other solvents whose densities were close to PS in order to ascertain that centrifugation did not alter the PS molecular weight characteristics appreciably. For very high molecular weight PS with $M_w \sim 2 \times 10^7$ and $M_w/M_n \sim 2$, high-speed centrifugation over long periods could separate out the high molecular weight fractions of the polymer by forcing those very large polymer coils to the bottom of the centrifuge tube. The centrifuge chamber was maintained at 10 °C as an additional precaution to minimize possible solvent evaporation that could alter the solvent composition.

Some physical properties of the solvents and polymers are summarized in Table I.

Experimental Apparatus. The light scattering spectrometer has been described elsewhere.[21] A Spectra Physics Model 165 argon ion laser operated at $\lambda_0 = 488$ nm, standard photon-counting equipment, and a Brookhaven Instrument (4n) 136-channel digital correlator were used to perform light scattering measurements. Only intensity–intensity time correlation functions, $G^{(2)}(K,t)$, with agreements of calculated and measured base lines of less than

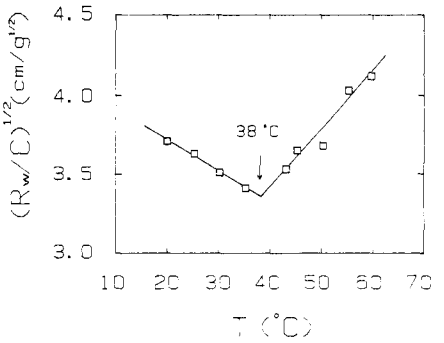

Figure 2. Search for the isorefractive matching temperature (T_M) using polystyrene ($M_w \sim 2 \times 10^6$, $C_{PS} = 3.15 \times 10^{-3}$ g/mL) and a mixed solvent of α-chloronaphthalene (CNA) and toluene (TOL) with volume fraction $\phi_{CNA} = 0.72$ measured at $\theta = 50°$. $T_M = 38$ °C.

0.1% were used for data analysis. Dynamic measurements were repeated at least twice using $\bar{\Gamma}$ values to check for reproducibility within 2–3%.

A capillary viscometer and a Brookfield cone/plate viscometer were used respectively to measure the viscosities of solvents and polymer solutions. A Parr precision density meter was used to measure the partial specific volumes of the PMMA probe in MS and in isorefractive, semidilute PS/MS solutions. We used an Abbe refractometer to measure the refractive index of MS at different solvent compositions at $\lambda_0 = 589$ nm.

Data Analysis Procedure. Electric field correlation functions were analyzed with CUMFIT (eq 15) and DEXP (eq 18). The CONTIN program kindly provided by Dr. S. W. Provencher was also used to analyze selected correlation functions.

IV. Results

Search for Matching Temperature. We used a PS ($M_w = 2 \times 10^6$, Pressure Chemical Co.)/MS ($\phi_{CNA} = 0.72$) solution at $C_{PS} = 3.15 \times 10^{-3}$ g/mL to locate the matching temperature T_M. The angular dependence of scattered light intensities at different fixed temeratures varying from 20° to 60° was measured.

As C and $K \rightarrow 0$, eq 3 can be rewritten as $n^2(dn/dC)^2C/R_{vv} \propto 1/M_w$ or

$$(R_{vv}/C)^{1/2} = B(1 + a_t|T - T_M|) \qquad (22)$$

where the constant B denotes a temperature independent quantity, a_t the temperatue coefficient of refractive index increment, and T_M the matching temperature. Figure 2 shows a plot of eq 22 revealing a sharp minimum scattered intensity at the matching temperature where $dn/dC \sim 0$. $T_m = 38 \pm 2$ °C for $\phi_{CNA} = 0.72$. Strictly speaking, the refractive index of polystyrene is slightly different from that of the solvent mixture because of preferential solvent interactions with polystyrene. What we have matched is the "solvated" polystyrene with the solvent mixture. An approximation was made for this search as we used an averaged R_{vv} at $\theta = 50°$ and $C = 3.15 \times 10^{-3}$ g/mL. However, the R_{vv} value at the finite scattering angle, i.e., $\theta = 50°$, instead of extrapolation to zero scattering angle should not affect the location of T_m. dn/dC for PS in MS with $\phi_{CNA} = 0.72$ is of the order of 0.003–0.005 for a 5° change in temperature from T_m, while for PMMA in MS $dn/dC = 0.089$. Thus, the PS matrix should not contribute significantly to the scattered intensity when compared with the PMMA probe. The ratio of $(dn/dC)^2$ for the PMMA probe and the PS matrix corresponds to a value of ~400. We used 1.68×10^{-3} g/mL PS ($M_w \sim 2 \times 10^7$) in MS at 38 °C and $\theta = 20°$ to check the negligible contribution in the scattering by PS under isorefractive conditions. A corresponding 1.2×10^{-4} g/mL PMMA/(PS/MS) solution having the same PS concentration and mixed solvent

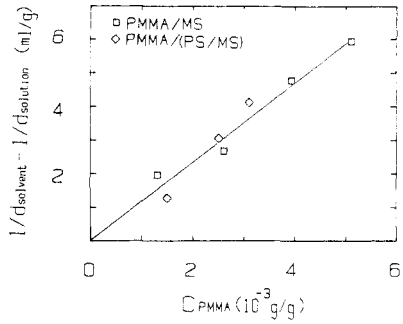

Figure 3. Specific volume of PMMA in MS and PS (C_{PS} = 1.68 × 10^{-3} g/mL)/MS (ϕ_{CNA} = 0.72) at 38 °C. The partial specific volume of PMMA can be calculated by $v_{PMMA} = v + (1 - C_{PMMA})[d(\Delta v)/dC]$, with the solution specific volume $v = 1/d_{soln}$ and $\Delta v = 1/d_{soln} - 1/d_{solv}$.

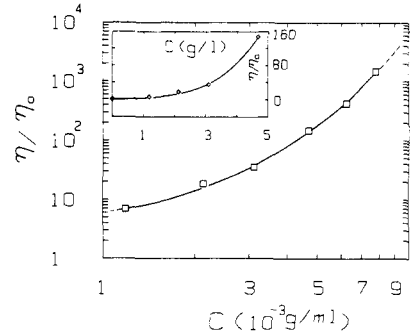

Figure 4. Viscosity of polystyrene ($M_w \sim 2 \times 10^7$) as a function of PS concentration in the isorefractive mixed solvent (ϕ_{CNA} = 0.72) at 38 °C. $\eta/\eta_0 = \exp[1.70C^{0.70}]$ with η_0 = 1.34 cP.

composition was used to measure the excess scattering intensity due to the PMMA probe. Only very weak and noisy correlations with background (A) accumulations of $\lesssim 10^6$ could be observed for the PS/MS solution (without the PMMA probe) after more than 2 h of accumulation time while intensity–intensity time correlations for the PMMA probe could be accumulated in less than 10 min with $A \gtrsim 10^7$. Therefore we assured ourselves that at 38 °C we had a reasonable MS with ϕ_{CNA} = 0.72 for isorefractive index matching with PS.

Partial Specific Volume and Refractive Index Increment. The refractive index of MS, as shown in Table I, was 1.601 at 488 nm and 38 °C. A standard (Brice Phoenix) differential refractometer with a resolution of 1 in 10^6 was not able to measure the dn/dC value for PMMA in MS because of the high refractive index of MS. We had to measure the partial specific volume of the polymer and calculate the dn/dC values. A Parr precision density meter was used to measure the densities of a set of PMMA solutions in MS and in PS (C_{PS} = 1.68 × 10^{-3} g/mL)/MS. Figure 3 shows $(1/d_{solv} - 1/d_{soln})$ vs. C_{PMMA} in MS and in PS/MS. The partial specific volume v_2 was calculated from the initial slope

$$v_2 = v + [d(\Delta v)/dC](1 - C_{PMMA}) \quad (23)$$

where $\Delta v = d_{soln}^{-1} - d_{solv}^{-1}$, $v = d_{soln}^{-1}$, and $v_2 = v_{PMMA}$.

By knowing v_2, we could calculate dn/dC with the Lorenz–Lorentz equation

$$dn/dC = v_2\left[\left(\frac{n_2^2 - 1}{n_2^2 + 2}\right) - \left(\frac{n_0^2 - 1}{n_0^2 + 2}\right)\right]\frac{(n_0^2 + 2)^2}{6n_0} \quad (24)$$

with n_2 and n_0 being the refractive index of the polymer (PMMA) and the solvent (MS or PS/MS), respectively. Although we had tried our best to remove possible bubbles in the solutions, the experimental error of the calculated dn/dC for PMMA in PS/MS was ~5%.

The refractive index increments of PMMA/MS and of PMMA/[PS (C_{PS} = 1.68 × 10^{-3} g/mL)/MS] were found to be −0.089 and −0.087, respectively, and could be considered to be the same within our experimental error limits.

Viscosity of PS/MS. Viscosities of semidilute PS/MS solutions were measured with a Brookfield cone/plate viscometer. The lowest shear rate for our cone/plate viscometer was 1.15 s^{-1}, which was not sufficiently low for us to determine the zero-shear rate viscosity. Fortunately, an estimated error of about 10% would not affect our conclusions. Figure 4 shows a plot of log η/η_0 vs. log C. We used an empirical formula

$$\eta/\eta_0 = \exp[aC^b] \quad (25)$$

to represent our experimental data. η and η_0 are the viscosities of the solution and solvent, respectively, C is the polymer concentration, and a and b are the fitting parameters.

Least-squares fitting of log (log η/η_0) vs. log C (g/L) yielded a = 1.7 and b = 0.70, which could be used to estimate the viscosity at any concentration of PS/MS in the semidilute regime within the experimental concentration range limit of $C \lesssim 10$ g/L.

Correlation Length of PS/MS in Semidilute Solution. One of the advantages in using a mixed solvent (TOL/CNA) is that by varying the solvent composition we can change the scattering power of PS from nearly zero (invisible) to appreciable (visible) in a more pronounced manner than by changing the temperature in a single solvent system. Semidilute PS solutions have been shown to obey the *limiting* scaling relation (eq 11) in both good and Θ solvents even though the magnitude of q is usually less than $^3/_4$, signifying a practical difficulty in reaching the limiting concentration range. We measured PS in TOL and used eq 10 to compute an average correlation length L as a function of concentration at $C > C^*$. Our results, as shown in Figure 5a, suggest a limiting slope q = 0.65 ± 0.05, which is in reasonable agreement with q = 0.67 ± 0.02 as reported in ref 22. At C_{PS} = 1.61 × 10^{-3} g/mL and 38 °C, the correlation length of PS solutions with MS at various solvent compositions were measured. Figure 5b shows the correlation length L of PS ($M_w \sim 2 \times 10^7$) as a function of solvent composition at 38 °C. The correlation length of isorefractive PS ($M_w = 2 \times 10^7$; C_{PS} = 1.61 × 10^{-3} g/mL) in MS with ϕ_{CNA} = 0.72 could be interpolated by means of Figure 5b to yield a value of 71 nm (with q = 0.65). By assuming TOL and MS to have comparable solvent quality, we could take q = 0.65 ± 0.05 for PS in MS and estimate experimentally over a concentration range $10^{-3} < C_{PS} < 10^{-2}$ (g/mL), as shown in Figure 5

$$L = 1.06C_{PS}^{-0.65} \text{ nm} \quad (26)$$

with C_{PS} expressed in g/mL. Equation 26 permits us to compute an average spatial correlation length of PS ($M_w \sim 2 \times 10^7$) in an isorefractive MS (ϕ_{CNA} = 0.72) at 38 °C as a function of concentration provided that 10^{-2} (g/mL) > C_{PS} > C_{PS}^* ~ 10^{-3} (g/mL).

Cooperative Diffusion of PS/MS. We measured the time correlation functions of PS/MS at C_{PS} = 1.61 × 10^{-3} g/mL, ϕ_{CNA} = 0, 0.45 and 1, and 38 °C. We were not able to observe only a single characteristic line width. Second-order CUMFIT yielded variances from 0.23 to 0.26 for ϕ_{CNA} = 0, with θ varying from 15° to 140°. One possible explanation for the large variance could be due to the crossover behavior; i.e., the PS concentration is only comparable to C^*. More details will be explored in our proposed model.

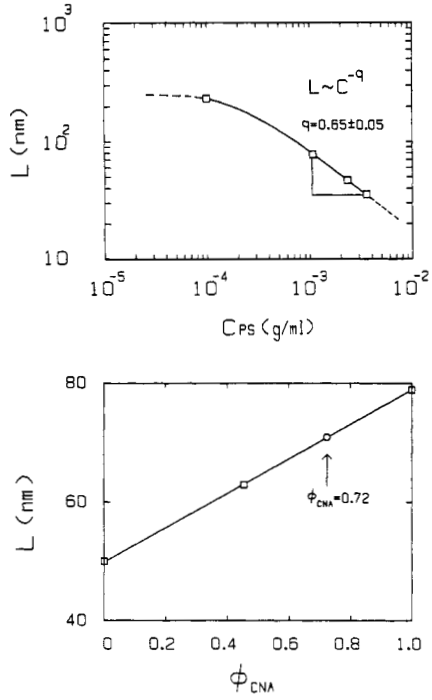

Figure 5. (a) Correlation length L of polystyrene ($M_w \sim 2 \times 10^7$) in toluene at 25 °C. At $C > C^*$, $q \simeq 0.65 \pm 0.05$. (b) Correlation length L of polystyrene ($M_w \sim 2 \times 10^7$) as a function of solvent composition in the mixed solvent (CNA/TOL) at 38 °C. The open circle denotes $L = 71$ nm at $\phi_{CNA} = 0.72$ and $C_{PS} = 1.61 \times 10^{-3}$ g/mL.

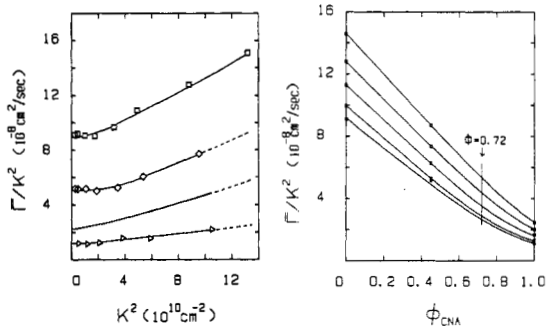

Figure 6. (a) Plots of $\bar{\Gamma}/K^2$ vs. K^2 for PS ($C_{PS} = 1.61 \times 10^{-3}$ g/mL) in MS at various fixed solvent compositions. We used only a second-order cumulants fit to *estimate* $\bar{\Gamma}$ values. $\mu_2/\bar{\Gamma}^2 \sim$ 0.23–0.26, with θ varying from 15° to 140°. R_g(PS) ~ 320 nm and M_w(PS) $\sim 2 \times 10^7$ at $\phi_{CNA} = 0.72$, $\lim_{K\to 0} \bar{\Gamma}/K^2 \sim 2.2 \times 10^{-8}$ cm²/s. The open squares denote PS in pure toluene ($\phi_{CNA} = 0$), the open diamonds denote PS in MS ($\phi_{CNA} = 0.45$), and the solid curve denotes PS in MS ($\phi_{CNA} = 0.72$), and the open triangles denote PS in pure α-chloronaphthalene ($\phi_{CNA} = 1$). (b) Plots of $\bar{\Gamma}/K^2$ vs. ϕ_{CNA} at various fixed K^2 values for PS ($C_{PS} = 1.61 \times 10^{-3}$ g/mL)/MS. $K^2 = 120 \times 10^9$, 87×10^9, 60×10^9, 35×10^9, and 20×10^9 cm^{-2} corresponding to the curves from the top to the bottom.

Figure 6a shows plots of $\bar{\Gamma}/K^2$ vs. K^2 for PS ($M_w \sim 2 \times 10^7$) at $C_{PS} = 1.61 \times 10^{-3}$ g/mL in MS with $\phi_{CNA} = 0$, 0.45, and 1. Corresponding $\bar{\Gamma}/K^2$ values at $\phi_{CNA} = 0.72$ could be estimated by interpolation of results measured at other solvent compositions. Figure 6b shows a typical interpolation curve based on $\bar{\Gamma}/K^2$ values measured at $\phi_{CNA} \neq 0.72$. In Figure 6a, we noted that $\bar{\Gamma}/K^2$ appeared to be relatively independent of K only at very small K ranges, i.e., for $KL \lesssim 1$. If we were to associate the time-dependent local concentration fluctuations in terms of the cooperative diffusion coefficient (D_c) with the spatial extension of local concentration fluctuations in terms of the correlation length (L), the higher K-power dependence could also

Table II
Molecular Parameters of a Fractionated PMMA Polymer in Dioxane, MS and PS/MS at 38 °C

solvent	dioxane	MS (ϕ_{CNA} = 0.72)	PS/MS (C_{PS} = 3.76 × 10⁻³ g/mL; ϕ_{CNA} = 0.72)
dn/dc, mL/g	0.0726	−0.089	−0.087
$M_{w,app}$, 10^6 g/mol		5.07	5.81
M_w, 10^6 g/mol	5.69	5.69	5.69 (6.5)[a]
α_a		0.034	−0.006 (0.034)[a]
$A_{2,app}$, 10^{-4} mol mL/g²		1.96	−0.11
A_2, 10^{-4} mol mL/g²	1.82	1.75	−0.11 (−0.098)[a]
$(R_g^2)_z^{1/2}$, nm	145	144	120

[a] If we assume α_a for PMMA in PS/MS to be the same as that for PMMA in MS, i.e., $\alpha_a = 0.34$, M_w becomes 6.5×10^6 and $A_2 = -0.098 \times 10^{-4}$ mol mL/g².

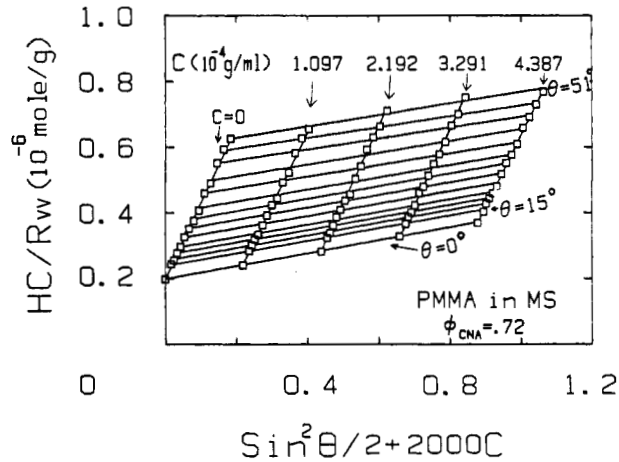

Figure 7. Zimm plot of PMMA (probe) in mixed solvent (ϕ_{CNA} = 0.72) at 38 °C. The results are listed in Table II.

suggest a composite nature of the local concentration fluctuations. However, at small KL (and KR_g) values, the composite nature of $\bar{\Gamma}$, i.e., a variance of 0.25, could be attributed to the polymer polydispersity. At $C \sim C^*$, we consider the origin of the two modes at $C \sim C^*$ comes from translational motions of the center of mass of those coils not yet entangled and a cooperative concentration fluctuation of entangled polymer coils. Again, we shall refer to the details in our proposed model as observed by laser light scattering for polymer semidilute solutions.

Static Properties of the PMMA/(PS/MS) System. A fractionated PMMA sample was characterized in dioxane, as shown in Figure 1. The results are being used to compare with the same fractionated PMMA polymer, in the absence of PS, in a mixed solvent at $\phi_{CNA} = 0.72$ (which is isorefractive with PS) and 38 °C. The Zimm plot results, as shown in Figure 7, are summarized in Table II. The difference between M_w and $M_{w,app}$ was used to compute α_a according to eq 7. We have noted only a small amount of the preferential adsorption effect. The important observation deals with measurements of the radius of gyration in the static properties and the time correlation function profile analysis of the probe by means of dynamic light scattering.

At $C_{PS} = 3.76 \times 10^{-3}$ g/mL, we used two PMMA probe concentrations. Figure 8 shows estimates of the apparent molecular parameters based on a two-point (PMMA) extrapolation using the Zimm plot. The measured molecular weight, second virial coefficient, and radius of gyration are listed in Table II.

In Table II was calculated the preferential adsorption coefficient (α_a) of PMMA in MS according to eq 6. $dn/d\phi$ at $\lambda_0 = 589$ nm was determined as a slope in a n_0 vs. ϕ_{CNA}

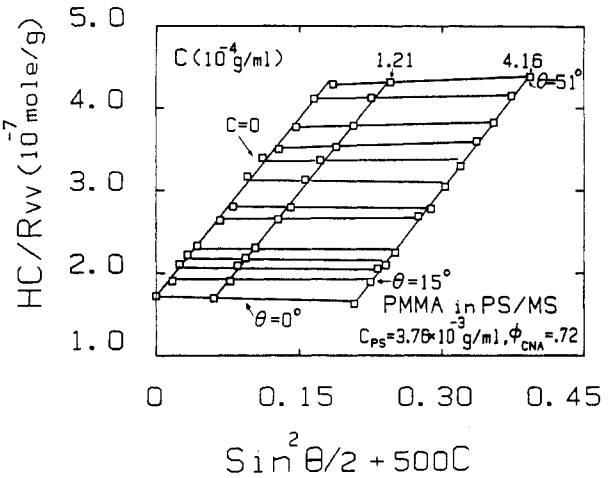

Figure 8. Zimm plot of PMMA (probe) in PS (C_{PS} = 3.76 × 10^{-3} g/mL)/MS (ϕ_{CNA} = 0.72) at 38 °C. The results are listed in Table II.

plot. We used the Lorenz–Lorentz equation to compute the refractive index of the mixed solvent n_0

$$\frac{n_0^2 - 1}{n_0^2 + 2} = \phi_{CNA}\left(\frac{n_{CNA}^2 - 1}{n_{CNA}^2 + 2}\right) + (1 - \phi_{CNA})\left(\frac{n_{TOL}^2 - 1}{n_{TOL}^2 + 2}\right) \quad (27)$$

and $dn/d\phi$ at λ_0 = 589 and 488 nm. The agreement between measured and computed $dn/d\phi$ values at λ_0 = 589 nm provided support for the $dn/d\phi$ values that we used in our analysis.

The parameters obtained for PMMA in PS/MS are quite revealing. The radius of gyration of PMMA in MS and PS (C_{PS} = 3.76 × 10^{-3} g/mL)/MS are respectively 144 and 120 nm; i.e., they are comparable. The PMMA probe shrinks slightly from MS to PS (C_{PS} = 3.76 × 10^{-3} g/mL)/MS since PMMA and PS are incompatible. With addition of PS to MS, the overall solvent quality becomes poorer for PMMA. The second virial coefficient A_2 changed from 1.75 × 10^{-4} to about −0.1 × 10^{-4} mol mL/g^2. If we assume α_a in PS (C_{PS} = 3.76 × 10^{-3} g/mL)/MS to be the same as α_a in MS, then $M_{w,app} \sim 6.5 \times 10^6$, a quantity about 13% higher than the true molecular weight of 5.7 × 10^6. However, the error involved in the refractive index increment measurements and in the two concentration Zimm plots of PMMA in PS/MS could be appreciable. Furthermore, we do not really have a valid justification to assume an identical α_a for PMMA in MS and in PS/MS. PMMA and PS are incompatible and the mixed solvent (CNA and TOL) is a good solvent for both PMMA and PS. The presence of an appreciable amount of PS has definitely changed the solvent quality of PS/MS for PMMA. Nevertheless, a dilute solution of PMMA in PS/MS is miscible. In summary, for PMMA in PS/MS, $M_w \approx M_{w,app}$. Only the PMMA coil size became slightly smaller; i.e., R_g (PMMA) changed from 144 to 120 nm. The expansion factor $\alpha = R_g/R_{g,\Theta}$ could vary from ~1.5 to 1 when the solvent quality changes from good to Θ.[12] In our case, $\alpha \sim 144/120 \sim 1.2$ and $A_2 \lesssim 0$ for PMMA in PS (C_PS = 3.76 × 10^{-3} g/mL)/MS($\phi_{CNA} \sim 0.72$), implying that although PS (C_{PS} = 3.76 × 10^{-3} g/mL)/MS is essentially a Θ solvent for PMMA, PMMA molecules are mainly surrounded by the small solvent molecules. Further increase of PS concentration should be treated with great care. We should also be aware of possible phase separation at high PMMA concentrations for the PS/MS solvent system since the presence of PMMA at finite concentrations also changes the PS behavior in the MS solvent system.

Table III
Structure and Dynamics of PMMA Probe and PS Matrix in MS at 38 °C

$10^4 C_{PMMA}$, g/mL	1.2	1.2	1.2
$10^3 C_{PS}$, g/mL	0	1.68	3.76
R_g*, nm	128	124	122
L, nm, in the absence of PMMA		69	40
η, cP	1.34	15	97
$10^9 D_T$, cm^2/s			
slow		2.10	0.70
fast		10.5	5.54
total	16.9	6.13	2.80
$10^{11} f R_g^2$,[a] cm^2			
slow		6.86	1.80
fast		7.62	2.92
total	3.36	7.08	4.89
f[b]	0.16		
R_h*,[c] nm			
slow		72	34
fast		(15)	(3.9)
total	101	(25)	(8.4)
R_h^*/R_g^*			
slow		0.58	(0.28)
fast			
total	0.79	(0.20)	(0.069)

[a] R_g* denotes R_g (C_{PMMA} = 1.2 × 10^{-4} g/mL) without extrapolation to infinite dilution. [b] Using $R_g \sim 144$ nm. [c] R_h* denotes an apparent hydrodynamic radius at C_{PMMA} = 1.2 × 10^{-4} g/mL.

Schematic Model for Polymer Semidilute Solutions. We have so far discussed experimental observations on the structure of our quaternary component system. Correlation function profile analysis of dilute PMMA probes in an isorefractive PS/MS solution has stimulated us to consider a schematic presentation of polymer structure and dynamics in semidilute solutions.

The reptation model[17] describes polymer entanglements in terms of tubes in which polymer chains could move. In a dilute polymer solution, each isolated polymer chain has its own translational diffusive motion of the center of mass and its internal modes. In a semidilute polymer solution, motions of each chain are affected by entangled neighboring polymer chains of comparable sizes. The polymer chain has a translational diffusive motion that essentially obeys the Stokes–Einstein relation even in the neighborhood of C^* provided that the solvent viscosity is replaced by the solution viscosity, as demonstrated by the experimental R_g, R_h, and η values listed in Table III. At sufficiently high concentrations, $C \gg C^*$, the polymer chain moves by reptation through a tube dynamically formed by entangled neighboring polymer chains. However, the tube is made up of entangled polymer coils in motion. Therefore, the reptation motion should be corrected for the tube length fluctuation effect. Semidilute polymer solutions are *not* polymer melts. In our case, the PS polymer coils occupy only ≲0.5% of space for $C \sim C^*$. In addition, polydispersity must necessarily play a very important role.

If the polymer coils in a semidilute solution form entanglements that are characterized by a mesh size, the low molecular weight fractions still have more oppotunity to move by translational diffusion. Thus, at least for a polydisperse high molecular weight polymer solution near the overlap concentration, we have a minimum of two characteristic times: a slow translational diffusion mode that obeys the Stokes–Einstein relation but uses the macroscopic solution viscosity as the solvent viscosity, and a fast cooperative diffusion (D_c) mode that is related to the polymer entanglements. At $C \sim C^*$, most polymer coils do not move by reptation since the tubes are not yet well

defined as in polymer melts.

In terms of a general linear viscoelastic theory for monodisperse flexible linear polymer melts, the translational dynamic mode has a characteristic time τ_C ($\sim M^{3.4}$)[23] and a Rouse-like process represented by a characteristic time τ_B ($\sim M^2$). In polymer melt rheology, stress relaxation plays a very important role. For entangled polymer coils, there are chain slippage through entanglement links ($\tau_X \sim MM_e$) and Rouse motion between entanglement links ($\tau_A \sim M_e^2$), with M_e being the entanglement molecular weight.

For semidilute polymer solutions, we can think of a screening (or correlation) length L that is related to the polymer mesh size and the cooperative diffusion coefficient D_c. If we have a large mesh size, we shall again observe coil internal motions between entanglement links at $KL \gg 1$. Thus, at very high polymer solution concentrations, the polymer matrix (PS/MS) is dominated by the cooperative diffusion coefficient and at $KL < 1$ a near single-exponential decay curve could result. At the intermediate concentration range and before individual translational motions of the center of mass of the polymer chains disappear, there are then two dominant motions: (1) a translational motion due essentially to the center of mass of the polymer chain and (2) a cooperative diffusive motion due to local concentration fluctuations of the pseudo polymer network, i.e., the entangled polymer coils, at $KL < 1$.

In our quaternary system, we can vary the PMMA polymer probe size and the PS polymer mesh size independently. In the presence of a PMMA polymer probe in PS/MS for KL(PS) < 1 and KR_g(PMMA) < 1, with R_g(PMMA) being the radius of gyration for the probe PMMA, we can observe the translational diffusion of the center of mass of PMMA *and* the localized concentration fluctuations of PS if both PMMA and PS have comparable scattering powers. Thus, the presence of a high-frequency mode for PMMA in the presence of invisible PS suggests a coupling of translational motions between PMMA and PS. However, contributions from translational motions of the center of mass of PS chains decrease with increasing PS concentrations at $C > C^*$. At KL(PS) < 1 and KR_g(PMMA) < 1, the PMMA polymer probe has two characteristic times, one related to the translational (or reptational if $C_{PS} \gg C_{PS}^*$) motion of the PMMA probe through entangled neighboring PS coils and the other transmitted mainly by the cooperative motions of PS coils. Then, the average integrated scattered intensity of the PMMA probe at KL(PS) < 1 and KR_g(PMMA) < 1 has at least two possible sources, i.e., the size of the PMMA probe and the entangled PS mesh size, even at small scattering angles in the absence of internal modes.

Our schematic model resembles the Ronca approach,[24] which predicts a complex and nonexponential dynamic structure factor $S(K,t)$. At sufficiently large KL ($\gg$1), $S(K,t)$ reflects internal motions between entanglement points. The prediction by Ronca is reasonable since by including a dynamic mode such as τ_A or τ_B the average characteristic line width can be represented as an expansion in K^2 with

$$\bar{\Gamma} = \bar{D}K^2(1 + fR_g^2K^2) \qquad (28)$$

which has the same form as eq 20 as proposed by Stockmayer and Schmidt.[25]

Figure 9 shows plots of the correlation length L for the PS matrix (in the absence of PMMA) and of the radius of gyration of PMMA as a function of PS concentration in an isorefractive mixed solvent of toluene and α-chloronaphthalene (ϕ_{CNA} = 0.72) at 38 °C. At high PS concentrations, A_2 becomes negative; i.e., the presence of an appreciable amount of PS which is incompatible with PMMA reduces the solvent quality of PS/MS and contracts R_g(PMMA). It should again be emphasized that with $A_2 < 0$ we should be careful with respect to the homogeneity of our polymer solution as phase separation could occur. Furthermore, the presence of PMMA should also change (reduce) the PS coil size and increase the effective magnitude of C^*.

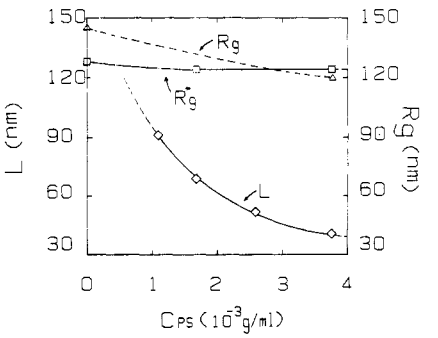

Figure 9. Radius of gyration (R_g) of the PMMA probe in PS/MS (ϕ_{CNA} = 0.72) and correlation length (L) of PS/MS (ϕ_{CNA} = 0.72) as a function of PS concentration at 38 °C. The open triangles denote the radius of gyration (R_g) at infinite dilution, the open squares denote the effective radius of gyration (R^*) at concentration $C_{PMMA} = 1.2 \times 10^{-4}$ g/mL, and the open diamonds denote the corresponding correlation length L.

Dynamic Light Scattering of the PMMA Probe in PS/MS. Time correlation functions of PMMA probes were measured at $KR_g^* \simeq$ 1–2 with R_g^* being the apparent radius of gyration for PMMA at a finite concentration in the PMMA dilution solution regime. The PMMA probe concentration was kept essentially at 1.2×10^{-4} g/mL. PS concentrations and corresponding molecular parameters such as L (for PS) and R_g^* (for PMMA) are listed in Table III.

PMMA in MS. Figure 10a shows a plot of the unnormalized net intensity–intensity time correlation function of 1.2×10^{-4} g/mL PMMA in MS (ϕ_{CNA} = 0.72) at 38 °C and θ = 20°. The unnormalized net intensity–intensity time correlation function for PMMA in MS behaves similarly as that in a pure solvent. A second-order cumulants fit (denoted by the solid curve in Figure 10a) fits the experimental data within our error limits. In order to show that our computed values of $\bar{\Gamma}$ and $\mu_2/\bar{\Gamma}^2$ are independent of methods of data analysis, we also fitted the same unnormalized net intensity–intensity time correlation function using a double-exponential (DEXP) fit. The use of a double-exponential fit here does not mean that now the correlation function has two characteristic line widths. It is used only to provide a mathematical representation of the experimental data and to compute the $\bar{\Gamma}$ and $\mu_2/\bar{\Gamma}^2$ values. Agreement of $\bar{\Gamma}$ and $\mu_2/\bar{\Gamma}^2$ values by two independent methods of data analysis confirms that we have obtained reliable $\bar{\Gamma}$ and $\mu_2/\bar{\Gamma}^2$ values. The results of our analysis are included in the caption of Figure 10a. Figure 10b shows a plot of log $b|g^{(1)}(t)|^2$ vs. delay time for the same PMMA in MS. The experimental data follow very nearly a single-exponential decay curve, which confirms our previous findings as shown in Figure 10a with $\mu_2/\bar{\Gamma}^2 \simeq$ 0.04.

PMMA in PS ($C_{PS} = 1.68 \times 10^{-3}$ and 3.76×10^{-3} g/mL)/MS. Figure 11a shows a typical unnormalized net intensity–intensity autocorrelation function of PMMA in PS ($C_{PS} = 1.68 \times 10^{-3}$ g/mL)/isorefractive MS. With $\tau_{max} \sim 0.1$ s, $G^{(2)}(t)$ is more susceptible to slow external perturbations and wiggles slightly at long delay times, although absolute deviations remain essentially the same

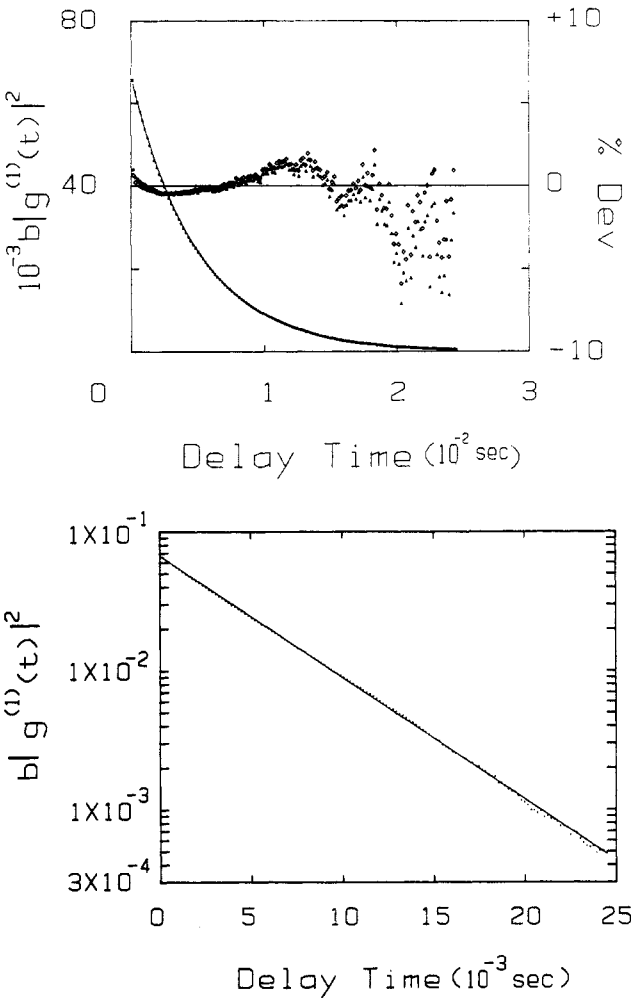

Figure 10. (a) Unnormalized net intensity–intensity time correlation function of PMMA in MS (ϕ_{CNA} = 0.72) at 38 °C. θ = 20°, C_{PMMA} = 1.20 × 10^{-4} g/mL. The solid curve is represented by $b^{1/2}|g^{(1)}(t)|$ = 0.26 exp(−103.8t + 176.7t^2). % Dev = 100-$(b^{1/2}|g^{(1)}(t)|_{exptl} - b^{1/2}|g^{(1)}(t)|_{calcd}/b^{1/2}|g^{(1)}(t)|_{exptl}$. The open diamonds denote a second-order cumulants fit $\bar{\Gamma}$ = 104 s^{-1}, $\mu_2/\bar{\Gamma}^2$ = 0.03. The solid triangles denote a double-exponential fit with $\bar{\Gamma}$ = 101 s^{-1}. A third-order cumulants fit yielded $\bar{\Gamma}$ = 102 s^{-1} and $\mu_2/\bar{\Gamma}^2$ = 0.04. Thus, we used the results of the third-order cumulants fit. (b) Plot of log $b|g^{(1)}(t)|^2$ vs. delay time for the same PMMA in MS as in part a. The figure is used to demonstrate near single-exponential behavior of a fairly narrow molecular weight distribution of PMMA in MS, in the absence of PS.

(about 5% in both Figures 10a and 11a).

In Figure 11a, we used the same PMMA concentration (C_{PMMA} = 1.2 × 10^{-4} g/mL) as in Figure 10a and the same MS composition (ϕ_{CNA} = 0.72). We measured the solution scattering at the same scattering angle (θ = 20°) and temperature (38 °C). The difference is that we added 1.68 × 10^{-3} g/mL of PS (M_w = 2.0 × 10^7) as shown in Figure 11a so that the solvent system is now made up of PS/MS and has an isorefractive polymer (PS) matrix with C (~1.68 × 10^{-3} g/mL) > C^* (~1 × 10^{-3} g/mL). The entangled PS has a correlation length L ~ 69 nm (in the absence of PMMA) while the PMMA probe has an effective radius of gyration R_g^* ~ 124 nm at C_{PMMA} ~ 1.2 × 10^{-4} g/mL. In the presence of a finite but low concentration of PMMA, L > 69 nm for the PS matrix and R_g > 124 nm for PMMA at infinite dilution. By using the CUMFIT and DEXP methods of data analysis, we obtained $\bar{\Gamma}_{CUM}$ = 42.4 s^{-1}, $(\mu_2/\bar{\Gamma}^2)_{CUM}$ = 0.51, $\bar{\Gamma}_{DEXP}$ = 40.1 s^{-1}, and $(\mu_2/\bar{\Gamma}^2)_{DEXP}$ = 0.47. The decrease of $\bar{\Gamma}$ from PMMA in MS to PMMA in PS/MS is expected since the presence of isorefractive PS greatly increases the macroscopic "solvent" viscosity for

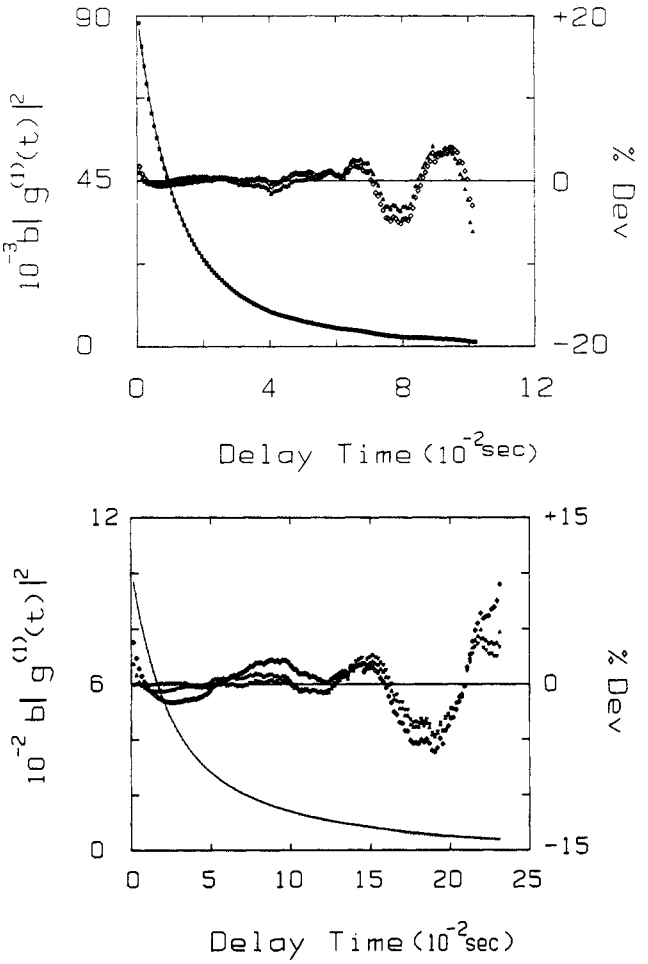

Figure 11. (a) Unnormalized net intensity–intensity time correlation function of PMMA in PS (C_{PS} = 1.68 × 10^{-3} g/mL)/MS (ϕ_{CNA} = 0.72) at 38 °C and θ = 20°. C_{PMMA} = 1.20 × 10^{-4} g/mL. The solid curve is represented by $b^{1/2}|g^{(1)}(t)|$ = 0.302[0.533 exp(−14.1t) + 0.467 exp(−74.8t)]. % Dev has been defined in Figure 10a. The open diamonds denote a third-order cumulants fit. The solid triangles denote a double-exponential fit. (b) Unnormalized net intensity–intensity time correlation function of PMMA in PS (C_{PS} = 3.76 × 10^{-3} g/mL)/MS (ϕ_{CNA} at 38 °C and θ = 20°. C_{PMMA} = 1.2 × 10^{-4} g/mL. Dev has been defined in Figure 10a. The solid curve is represented by $b^{1/2}|g^{(1)}(t)|$ = 0.321[0.575 exp(−4.77t) + 0.425 exp(−36.3t)]. The open diamonds denote a third-order CUMFIT, the solid triangles denote a DEXP fit and the inverted solid triangles denote a CONTIN fit. Long delay time fluctuations in % Dev are experimental slow instabilities of the instrument. Only deviations in the short-delay-time range show how CONTIN fits the experimental data much better.

the PS/MS "solvent" system. The dramatic increase in the variance from 0.04 for PMMA in MS to ~0.5 for PMMA in PS (C_{PS} = 1.68 × 10^{-3} g/mL)/MS requires careful examination. To begin with, our methods of data analysis have yielded a reasonably reliable value for $\bar{\Gamma}$ but perhaps an underestimate of $\mu_2/\bar{\Gamma}^2$. The high variance value clearly suggests that we have either a very broad unimodal characteristic line-width distribution or a multimodal characteristic line-width distribution. In a semdilute polymer solution with C_{PS} (~1.68 × 10^{-3} g/mL) ≳ C_{PS}^* (~1 × 10^{-3} g/mL), the dilute optical PMMA probe (C_{PMMA} = 1.2 × 10^{-4} g/mL ≪ C_{PMMA}^*) could be experiencing the dynamical effects produced by the PS coils. Thus, even at KL(PS) < 1 and KR_g(PMMA) < 1 we could expect a broadening of the characteristic line-width distribution which might be attributed to the translational motion of the center of mass of PMMA probe molecules in the presence of entangled PS coils. In other words, with dilute PMMA probes, we are, in fact, measuring the rep-

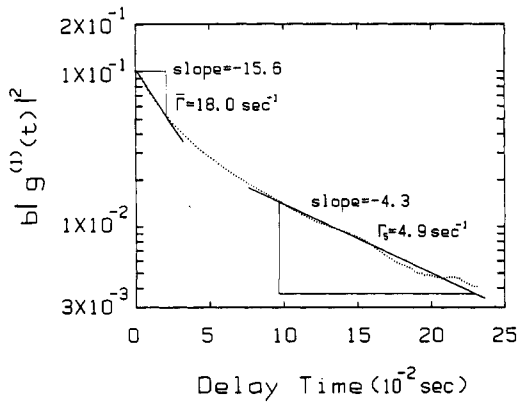

Figure 12. Plot of log $b|g^{(1)}(t)|^2$ vs. delay time for the same PMMA in PS (C_{PS} = 3.76 × 10^{-3} g/mL)/MS (ϕ_{CNA} = 0.72) at 38 °C and θ = 20°. This is the same correlation function as in Figure 11b. Deviation from a linear curve denoting single-exponential behavior is undeniable. A break in the curve is suggested. Initial slope shows $\bar{\Gamma} \sim 18$ s^{-1} and the long-time limit is compatible with $\Gamma_s \sim 4.9$ s^{-1}.

tational self-diffusion coefficient D_s of PMMA with $D_s \sim M^{-2}$ instead of $D \sim M^{-\alpha}$ and $\alpha \sim 0.5$–0.6. Thus, an increase in the $\mu_2/\bar{\Gamma}^2$ value is not surprising. In order to confirm the findings of a large $\mu_2/\bar{\Gamma}^2$ value for the PMMA probe in the presence of an isorefractive PS matrix, we present another unnormalized net intensity–intensity time correlation function for 1.2 × 10^{-4} g/mL PMMA in PS (C_{PS} = 3.76 × 10^{-3} g/mL)/MS (ϕ_{CNA} = 0.72) at 38 °C and θ = 20°, as shown in Figure 11b. By increasing the PS concentration, we have reduced the correlation length L (~40 nm) of the PS matrix; yet, the PMMA coil size remains essentially unchanged with R_g*(PMMA) ~ 122 nm. It should be noted that at C_{PS} = 3.76 × 10^{-3} g/mL, R_g*(PMMA) [~122 nm] is greater than L(PS) [~40 nm] while at C_{PS} = 1.68 × 10^{-3} g/mL, R_g*(PMMA) (~124 nm) and L(PS) (~69 nm) are more comparable in size. Thus, we may expect differences under the two conditions, which will be discussed later. Nevertheless, results of analysis of the third-order CUMFIT and DEXP methods suggest similar broadening of the variance $\mu_2/\bar{\Gamma}^2$ as shown in Figure 11a.

On closer examination, we note that there is a quantitative difference in the unnormalized net intensity–intensity time correlation function between Figures 10a and 11. Figure 12 shows a log $b|g^{(1)}(t)|^2$ vs. delay time plot for the same PMMA solution as shown in Figure 11b, i.e., 1.2 × 10^{-4} g/mL PMMA in PS (C_{PS} = 3.76 × 10^{-3} g/mL)/MS (ϕ_{CNA} = 0.72) at 38 °C and θ = 20°. The near single-exponential behavior of Figure 10b is no longer applicable to the experimental data (denoted by dots) in Figure 12. Instead, we have noted a break in the curve, suggesting a minimum of two peaks in the characteristic line-width distribution. Now, the two peaks presented by the DEXP method of data analysis begin to have a real physical meaning, at least semiquantitatively. If we can indeed succeed in obtaining a Laplace inversion of the net intensity–intensity time correlation function, especially when the method of data analysis does not require an a priori knowledge of the form of the characteristic line-width distribution function, the multimodal behavior, if present, would suggest dynamical effects in addition to single-coil translational diffusion.

Figure 13 shows a typical characteristic line-width distribution function $G(\Gamma)$ based on the Laplace inversion method developed by Provencher, commonly known as CONTIN for PMMA in PS (C_{PS} = 1.68 × 10^{-3} g/mL)/isorefractive MS at θ = 20°. We could resolve $G(\Gamma)$ to be

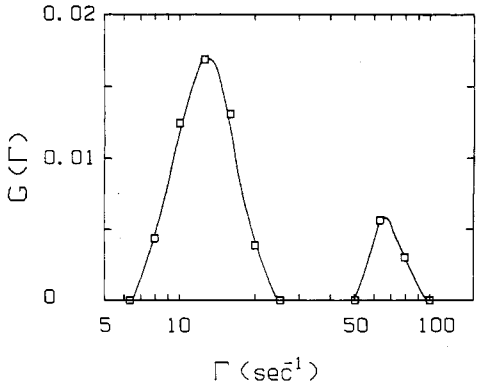

Figure 13. Plot of $G(\Gamma)$ vs. Γ using the CONTIN method of analysis for the same system as in Figure 11a. C_{PS} = 1.68 × 10^{-3} g/mL. A_s = 0.49, $\bar{\Gamma}_s$ = 13.7 s^{-1}, $\mu_{2s}/\bar{\Gamma}_s^2 \sim 0.05$; A_f = 0.47, $\bar{\Gamma}_f$ = 64.7 s^{-1}, $\mu_{2f}/\bar{\Gamma}_f^2 \sim 0.01$; A_x = 0.04, $\bar{\Gamma}_x$ = 654 s^{-1}, $\mu_{2x}/\bar{\Gamma}_x^2 \sim 0.04$. The high-frequency x component is neglected. For details see Table IV on results of CONTIN analysis.

(at least) bimodal without an a priori assumption on the form of $G(\Gamma)$ by the CONTIN algorithm. The variances of the slow mode and the fast mode were 0.05 and 0.01, respectively. The corresponding average characteristic line widths were 13.7 and 67.4 s^{-1}. The intensity contributions were close to 1:1. The multimodal characteristic in $G(\Gamma)$ was present for the PMMA probe in PS (C_{PS} = 1.68 × 10^{-3} and 3.76 × 10^{-3} g/mL)/isorefractive MS over the entire scattering angular range of our studies. Typical results of our analysis are presented in Table IV.

As CONTIN revealed the existence of a minimum of two characteristic modes in PMMA probe diffusion, we also tried to examine whether the time correlation function profile could be interpreted by other means, such as a very broad unimodal characteristic line-width distribution. With the proposed schematic model we could estimate the strength and location of both peaks from existing experimental results and thereby test the outcome of time correlation function profile analysis under favorable conditions where the amplitudes of the two peaks are comparable and the location in Γ-space sufficiently far apart. Thus, we can conclude that the CONTIN algorithm has provided strong support for at least a bimodal behavior in $G(\Gamma)$.

It is important to emphasize the limitation of the Laplace inversion method of data analysis even for very precise time correlation functions. We have taken particular care not to use a floating base-line method of data analysis, i.e., not to use the base line A in eq 12 as a fitting parameter. Our measured and computed base lines agree to within 0.1% before the net time correlation function $|g^{(1)}(t)|$ is accepted for data analysis. The slow fluctuations that appear as wiggles in $g^{(1)}(t)$ also present some problems. Although we consider them (see Figures 10a and 11a) to be experimental artifacts, not related to our search for the dynamical motions of polymer coils in semidilute solutions, nevertheless, the modulations, to a certain extent, interfere with our data analysis. If we accept that $|g^{(1)}(t)|$ can provide only limited resolution for $G(\Gamma)$ and the $G(\Gamma)$ results, if multimodal, are qualitative, useful information can be obtained from such analysis. In Table IV, we have included CONTIN results of data analysis using different upper (Γ_{max}) and lower (Γ_{min}) bounds in the $G(\Gamma)$ distribution. For example, at θ = 20° and for PMMA in 1.68 × 10^{-3} g/mL PS/MS (ϕ_{CNA} = 0.72) at 38 °C, three different values of Γ_{min} were tried. The results show a minimum of two peaks (denoted by slow and fast peaks as shown in Figure 13) and the presence of a possible third (X) peak. The locations of $\bar{\Gamma}_s$ and $\bar{\Gamma}_f$ are quite reproducible even if

Table IV
Correlation Function Profile Analysis Using the CONTIN Method

A. 1.2×10^{-4} g/mL PMMA in 1.68×10^{-3} g/mL PS Isorefractive with MS ($\phi_{CNA} = 0.72$) at 38 °C

θ, deg	20	20	20	30	30
Γ_{min}, s^{-1}	1	2	0.01	2	0.5
Γ_{max}, s^{-1}	2×10^3	2×10^3	2×10^3	3×10^3	3×10^5
α_C[a]	1.28×10^{-5}	1.28×10^{-5}	2.42×10^{-5}	2.5×10^{-5}	2.46×10^{-5}
PJ[b]	0.322	0.311	0.563	0.767	0.518
slow peak					
$\bar{\Gamma}_s$, s^{-1}	13.9	13.7	14.8	59.5	59.8
$\mu_{2s}/\bar{\Gamma}_s^2$	0.06	0.05	0.14	0.10	0.10
A_s	0.99	0.49	0.50	0.60	0.61
fast peak					
$\bar{\Gamma}_f$, s^{-1}	67.8	67.4	68.5	248	249
$\mu_{2f}/\bar{\Gamma}_f^2$	0.01	0.01	0.03	0.03	0.02
A_f	0.47	0.47	0.46	0.35	0.35
third (x) peak[c]					
$\bar{\Gamma}_x$, s^{-1}	7×10^2	7×10^2	7×10^2	$\sim 1.7 \times 10^3$	$\sim 1.7 \times 10^3$
$\mu_{2x}/\bar{\Gamma}_x^2$	~0.01	~0.04	~0.04	~0.01	~0.01
A_x	0.04	0.04	0.04	0.04	0.03

B. 1.2×10^{-4} g/mL PMMA in 3.76×10^{-3} g/mL PS Isorefractive with MS ($\phi_{CNA} = 0.72$) at 38 °C

θ, deg	20	20	30	30
Γ_{min}, s^{-1}	0.05	0.1	0.5	0.2
Γ_{max}, s^{-1}	1×10^3	5×10^3	5×10^3	3×10^3
α_C[a]	1.57×10^{-4}	1.57×10^{-4}	1.22×10^{-5}	4.39×10^{-5}
PJ[b]	0.231	0.337	0.259	0.894
slow peak				
$\bar{\Gamma}_s$, s^{-1}	7.71	7.20	8.64	8.98
$\mu_{2s}/\bar{\Gamma}_s^2$	0.49	0.38	0.12	0.22
A_s	0.68	0.66	0.39	0.38
fast peak				
$\bar{\Gamma}_f$	48.6	47.8	68.6	70.7
$\mu_{2f}/\bar{\Gamma}_f^2$	0.02	0.04	0.02	0.06
A_f	0.29	0.31	0.47	0.47
third peak[c]				
$\bar{\Gamma}_3$, s^{-1}	514	535	365	412
$\mu_{23}/\bar{\Gamma}_3^2$	<0.01	~0.02	~0.02	~0.01
A_3	~0.03	~0.03	~0.10	~0.10
fourth peak[d]				
$\bar{\Gamma}_4$, s^{-1}			2×10^3	~0.10
$\mu_{24}/\bar{\Gamma}_4^2$			0.02	~0.10
A_4			~0.04	~0.04

[a] α_C is a parameter in the CONTIN method indicating goodness of fit; smaller values are better. [b] PJ denotes probability to reject the fitting result. [c] The third peak is a consequence of the CONTIN method. It suggests the possibility of additional high-frequency components as observed by light scattering at KR_g(PMMA) ~1. The magnitudes are qualitative at best. [d] $\sum A_i = 1$.

we use the DEXP method of data analysis as listed in Table V. It appears that DEXP fits the time-correlation function, except for the initial portion, which contains some high-frequency components, as shown in the deviation plots of Figure 11b; i.e., the CONTIN result (with the third frequency (X) peak) fits the initial decay of the time correlation function better than the DEXP curve. If we were to ignore the small high-frequency contribution, the characteristic line-width distribution of the PMMA probe (at $KR_g \lesssim 1$) still contains two peaks. The amplitudes and the line width of the two peaks agree quite well when either the CONTIN or DEXP methods of data analysis are used.

Following the recent analysis by Lodge et al.[27] we constructed an effective net intensity–intensity time correlation function $[G^2(\tau)/A - 1]$ by using the MWD (with $M_w/M_n \sim 1.2$) estimated from $G(\Gamma)$ of the time correlation function as shown in Figure 10a and the relations $\Gamma = DK^2$ and $D \sim M^{-2}$ (instead of $D \sim M^{-0.55}$) for the x axis of the new $G(\Gamma)$ but retaining the y amplitudes of the original $G(\Gamma)$. The simulated net intensity–intensity time correlation functions (without and with ~0.1% random noise together with an appropriate shift in time scale to reflect the viscosity change) were analyzed by the CONTIN method and a third-order cumulants fit. The main conclusions from the analysis using simulated data can be summarized as follows. In the presence of noise, the CONTIN method could produce an additional spurious high-frequency peak of small amplitude. However, based on the CONTIN method, the resulting $\bar{\Gamma}$ values for the main peak agreed to within a few percent of the input values while the $\mu_2/\bar{\Gamma}^2$ values for the main peak exhibited a narrowing effect but showed magnitudes (~1–1.2) close to the inputs (~1.5). The third-order cumulants fit substantially underestimated the $\mu_2/\bar{\Gamma}^2$ values. We were not able to pro-

Table V
Comparison of $\bar{\Gamma}_{overall}$, $\bar{\Gamma}_{s+f}$, $\bar{\Gamma}_s$, and $\bar{\Gamma}_f$ from CONTIN with $\bar{\Gamma}_{DEXP}$, Γ_s, and Γ_f from DEXP

θ, deg	20	30	20	30
C_{PS}, g/mL	1.68×10^{-3}	1.68×10^{-3}	3.76×10^{-3}	3.76×10^{-3}
CONTIN				
$\bar{\Gamma}_{overall}$, s^{-1}	64.0	199	35.7	153
$\bar{\Gamma}_{s+f}$, s^{-1}	40.3	129	19.9	41.4
$\bar{\Gamma}_s$, s^{-1}	13.9	59.8	7.71	8.64
A_s	0.49	0.61	0.68	0.39
$\bar{\Gamma}_f$, s^{-1}	67.8	249	48.6	68.6
A_f	0.47	0.35	0.29	0.47
DEXP				
$\bar{\Gamma}_{DEXP}$, s^{-1}	42.2	127	18.2	47.4
Γ_s, s^{-1}	14.1	44.2	4.77	9.04
A_s	0.53	0.54	0.58	0.45
Γ_f, s^{-1}	74.8	223	36.3	78.7
A_f	0.47	0.46	0.42	0.55

[a] $\bar{\Gamma}_{overall}$ represents the measured average line width from the CONTIN method of data analysis with the presence of a third peak. We take $A_s + A_f = 1$ instead of $A_s + A_f + A_x = 1$ for comparison of CONTIN results with DEXP fits. [b] $\bar{\Gamma}_{s+f} = (A_s\bar{\Gamma}_f + A_f\bar{\Gamma}_f)/(A_s + A_f)$ (instead of $\bar{\Gamma}_{overall} = \sum A_i\bar{\Gamma}_i/\sum A_i$).

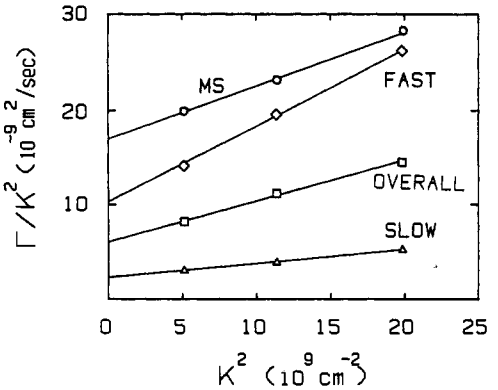

Figure 14. Plots of Γ/K^2 vs. K^2 for PMMA ($C_{PMMA} = 1.2 \times 10^{-4}$ g/mL) in PS ($C_{PS} = 1.68 \times 10^{-3}$ g/mL)/MS ($\phi_{CNA} = 0.72$) at 38 °C using the double-exponential method of analysis. $D = K \rightarrow 0$ $\bar{\Gamma}/K^2$ (10^{-8} cm^2/s): MS, 1.7; fast, 1.1; slow, 0.21; overall, 0.61. MS denotes PMMA ($C_{PMMA} = 1.2 \times 10^{-4}$ g/mL) in MS ($\phi_{CNA} = 0.72$) using a third-order cumulants fit.

duce an artificial bimodal distribution of comparable amplitudes in $G(\Gamma)$ using a broad $G(\Gamma)$ distribution as input and the CONTIN method of data analysis in the presence of a reasonable amount of random noise. We shall now try to identify the nature of these two peaks.

Time correlation functions of PMMA in MS were quite different from those in PS/MS and could be analyzed with the second-order cumulants fitting procedure, yielding $\mu_2/\bar{\Gamma}^2 = 0.04$ at $\theta = 20°$. Plots of $\bar{\Gamma}/K^2$ vs. K^2 are shown in Figure 14. The results, according to eq 20, are listed in Table II. If we took R_g(PMMA) = 144 nm, we obtained $f \sim 0.16$, in amazing agreement with the predicted expectation value of $^1/_6$ without preaveraging for random coils in a good solvent. Thus, the use of mixed solvent can be well characterized. Furthermore, it gives us the flexibility of observing the structure and dynamics of both the entangled polymer coils (PS/MS) and the polymer probe (PMMA).

Figure 14 shows the DEXP fitting results of dilute PMMA in a PS ($C_{PS} = 1.68 \times 10^{-3}$ g/mL)/MS ($\phi_{CNA} = 0.72$) solution. In plots of $\bar{\Gamma}/K^2$ vs. K^2 for the slow mode, the fast mode, and the overall average line width $\bar{\Gamma}$, we obtained three straight lines, each obeying eq 28. $\bar{\Gamma}$ [$\equiv(A_s\Gamma_s + A_f\Gamma_f)$] is the intensity weighted sum of Γ_s and Γ_f. Thus, the weighting factor, i.e., the scattered light intensity, has an angular dependence if contributions from the fast (f) and the slow (s) modes come from sources that have interference effects. The fast mode had a strong K^2 dependence. CONTIN showed that with increasing K values the peaks became more difficult to separate. At $C_{PS} \simeq 1.68 \times 10^{-3}$ g/mL, the center of mass translational diffusion coefficient D_T of the slow mode for the PMMA probe was ~8 times smaller than D_T of PMMA in the mixed solvent at the same temperature (38 °C), while the viscosity of PS/MS was ~10 times higher than that of the mixed solvent. From static light scattering measurements, we knew that the sizes of the PMMA probe in MS and PS/MS, as listed in Table III, were almost the same with little shrinkage of PMMA in PS/MS. If we were to compute an apparent hydrodynamic radius R_h* with the Stokes–Einstein relation and PS/MS viscosity, we would obtain R_{hs}* ~ 72 nm and R_h*(overall) ~ 25 nm with the subscript hs denoting the hydrodynamic size computed from the slow mode. The results are summarized in Table III.

If we did not consider the origin of scattering from the PMMA probe, we would have attempted to compute an apparent hydrodynamic radius from the average overall characteristic line width ($\bar{\Gamma}$), yielding an incorrect R_h* ~ 25 nm. As R_h*/R_g* varied from 101/128 ~ 0.78 for PMMA in MS to 25/124 ~ 0.20 overall for PMMA in PS ($C_{PS} = 1.68 \times 10^{-3}$ g/mL)/MS, it would appear that the Stokes–Einstein relation did not hold at all for PMMA in PS ($C_{PS} = 1.68 \times 10^{-3}$ g/mL)/MS. However, in view of the composite nature of the intensity–intensity time correlation function, we propose a different conclusion; i.e., the failure of the Stokes–Einstein relation is only marginal with R_{hs}*/R_g* ~ 72/124 ~ 0.58. More specifically, the change in "solvent" viscosity from $\eta_{MS} = 1.34$ cP to $\eta_{PS/MS}$ ($C_{PS} = 1.68 \times 10^{-3}$ g/mL) = 15 cP, an increase by a factor of ~10, is comparable to the ratio of D_T [$\equiv \lim_{K\rightarrow 0} \bar{\Gamma}/K^2$] ~ 1.7×10^{-8} cm^2/s for PMMA in MS and the slow mode, where D_{slow}(PMMA) [$\equiv \lim_{K\rightarrow 0} \Gamma_{slow}/K^2$] ~ 2.1×10^{-9} cm^2/s for PMMA in PS ($C_{PS} = 1.68 \times 10^{-3}$ g/mL).

The appreciable K^2 dependence in a Γ_s/K^2 vs. K^2 plot suggests that we did not have a clear separation in the dynamic modes. Some internal mode contributions remain in Γ_s, especially at higher K values. It should also be noted that in using DEXP we have completely ignored the polydispersity effect in the translational motions of PMMA in PS/MS. Even for a narrow molecular weight distribution of PMMA ($M_w/M_n \lesssim 1.2$), the slow mode has a variance of ~0.4 as listed in Table IVB for the probe PMMA in PS ($C_{PS} = 3.76 \times 10^{-3}$ g/mL)/MS at 38 °C. Thus, the slight variation of a K^4 dependence for Γ_s/K^2 vs. K^2 in this semiquantitative (DEXP) method of analysis is not surprising. The similar trend in the K dependence for $\bar{\Gamma}$ (overall; PMMA in PS ($C_{PS} = 1.68 \times 10^{-3}$ g/mL)/MS) and $\bar{\Gamma}$ (MS; PMMA in MS) suggests further that the internal motions of PMMA remain essentially unchanged. In the limit $K \rightarrow 0$, PMMA does not have a simple unimodal characteristic line-width distribution. It has additional high-frequency components that are represented qualitatively by Γ_f. Two aspects of this interpretation require further reiteration: (1) The slow mode has a broader characteristic line-width distribution with $\mu_2/\bar{\Gamma}^2 \sim 0.4$ (as estimated by CONTIN) at $C_{PS} = 3.76 \times 10^{-3}$ g/mL. This value for the variance of the slow mode is compatible with the molecular weight polydispersity index ($M_w/M_n < 1.2$, as determined by laser light scattering for the PMMA probe in dioxane) if we accept an increase in the α value for PMMA in the PS matrix at $C_{PS} \sim 4C_{PS}$* with D_{slow} proportional to $M^{-\alpha}$ and $0.6 < \alpha < 2$. As the translational diffusion coefficient D_T of polymer coils in a fairly good solvent in the dilute solution regime is proportional to $M^{-\alpha}$ with $\alpha_D \sim 0.55$–0.6 and the self-diffusion coefficient D_s of polymer coils in the semidilute solution limit is proportional to $M^{-\alpha_s}$ with $\alpha_s \sim 2$, the increase in $\mu_2/\bar{\Gamma}^2$ from ~0.04 to ~0.4 is at least in the right direction. (2) It is an oversimplification to represent the motions of entangled PS coils that are coupled to the PMMA probe by using only Γ_f. This approximation should improve with increasing PS concentration. At $C_{PS} = 1.68 \times 10^{-3}$ g/mL, the PS concentration is sufficiently close to the overlap concentration such that both the translational motion of the center of mass of PS and the local concentration fluctuations of entanglement links as denoted by the cooperative diffusion coefficient D_c are present. Thus, additional dynamics originates not only from motions of entangled polymer links but also from individual PS polymer coils. Γ_f has a higher value than anticipated perhaps because the internal modes of large PS ($M_w \sim 2 \times 10^7$) coils may have also contributed toward the coupling between PMMA and PS over the angular range of our studies.

We have attributed the origin of the fast component as due mainly to motions of entangled PS coils. Even though

PS coils were made isorefractive with the mixed solvent and were optically invisible, the entangled pseudonetwork could couple its motions with the PMMA probe. $\Gamma_f/K^2 \sim 1 \times 10^{-8}$ cm^2/s, as shown in Figure 14, could be found to be of the same order of magnitude as 2×10^{-8} cm^2/s, as shown in Figure 6a.

At $C_{PS} = 3.76 \times 10^{-3}$ g/mL, the size of the PMMA probe remains essentially the same ($R_g^* \sim 122$ nm). L (=40 nm) becomes smaller. The Stokes–Einstein relation has failed, as reported by others.[13] The slow mode representing the translational motion of the PMMA probe through the tube formed by entangled neighboring PS coils has not decreased in proportion to the increase in overall solvent viscosity from 15 to 97 cP.

Phillies[31] and Pusey et al.[32] have derived a bimodal time correlation function of three-component solutions containing a solvent and two interacting particles based on coupled linear diffusion equations

$$\frac{d}{dt}a_A(r,t) = D_A\nabla^2 a_A(r,t) + D_{AB}\nabla^2 a_B(r,t) \quad (29a)$$

$$\frac{d}{dt}a_B(r,t) = D_{BA}\nabla^2 a_A(r,t) + D_B\nabla^2 a_B(r,t) \quad (29b)$$

where $a_A(r,t)$ and $a_B(r,t)$ are the concentrations of particles A and B, respectively, at position r and time t and D_A, D_B, D_{AB}, and D_{BA} are multicomponent mutual diffusion coefficients. For a special case whereby A is dilute but scatters very strongly and B is concentrated but almost invisible, and when the mode coupling terms are ignored[31]

$$g^{(1)}(K,t) \simeq \left(I_A - \frac{D_{BA}}{D_B - D_A}I_{AB}\right)\exp(-D_AK^2t) + \left(I_B + \frac{D_{BA}}{D_B - D_A}I_{AB}\right)\exp(-D_BK^2t) \quad (30)$$

where D_A is now the self-diffusion of A and D_B is the mutual diffusion coefficient of B in the absence of A; I_A and I_B are respectively the scattering intensities of A and B, including interference effects. The dynamic scattering term I_{AB} vanishes if either species scatters no light.

In eq 30 the self-diffusion mode of the probe A is a dominating term for polymer probe diffusion provided that the hydrodynamics is governed by eq 29.

Unfortunately, eq 30 is not applicable to our observation of a bimodal characteristic time distribution of comparable intensity magnitudes[33] at $KR_g \lesssim 1$ (where internal motions cannot be observed) for the quaternary component solution (PMMA probe in PS/MS). Thus, the presence of polymer pseudonetworks seems to introduce local structural characteristics that are not included in eq 29. A more detailed theory must necessarily include effects of polydispersity and relationships between polymer size and entanglement mesh dimension, as well as dynamics of disentanglements together with polymer internal motions.

V. Conclusion

We have used a quaternary component probe/matrix polymer solution to investigate how the probe (PMMA) diffuses in semidilute polymer (PS) solutions. Absolute light scattering intensity measurements have shown that our incompatible polymer pair (PMMA/PS) forms a stable solution that can be characterized completely, in agreement with earlier findings of Kuhn et al. for the PS/PMMA pair in benzene.[26]

By changing the solvent composition of the mixed solvent (CNA/TOL), we were able to study the structure and dynamics of PS in the semidilute solution regime. Properties of the PS polymer matrix can be interpolated to the matching solvent composition where PS becomes invisible. The correlation length (L) and the corresponding cooperative diffusion coefficient were measured. Internal motions of PS in semidilute solutions appear and have been taken into account in our discussion.

Photon correlation function measurements were performed at the small-scattering-angle regime ($R_g^*K = 1$–2). CONTIN analysis shows the existence of at least two relaxation modes for the PMMA probe where internal modes should be unimportant, as demonstrated by the PMMA/MS result at $\theta = 20°$. A double-exponential (DEXP) method of data analysis for the correlation function profiles was used to support the more detailed CONTIN analysis showing reasonable agreement in the amplitude and position of both the slow and the fast modes. By combining static and dynamic results, we were able to identify the origin of various dynamical motions based on a schematic model for polymer semidilute solutions. The PMMA probe has a translational motion of center of mass and an internal mode which becomes appreciable for $KR_g > 1$. In the PS matrix, PMMA feels the PS motions resulting in bimodal $G(\Gamma)$ even at very small scattering angles. The results are summarized in Table III. At $C_{PS} = 1.68 \times 10^{-3}$ g/mL $> C_{PS}^*$, the PMMA probe has a slow translational diffusion motion which has not deviated appreciably from the Stokes–Einstein relation with $\mu_2/\bar{\Gamma}^2 \sim 0.06$ for the slow mode, as listed in Table IVA, comparable to $\mu_2/\bar{\Gamma}^2 \sim 0.04$ for PMMA in MS. R_{hs}^*/R_g^* ($\sim$0.58) appears to have a reasonable value. However, the presence of a fast mode with magnitudes comparable to D_c is undeniable. It would be interesting to speculate that in a *rigid* matrix of similar mesh size, the bimodal characteristic should disappear, leaving only translational motions of the PMMA probe at $KR_g < 1$. At $C_{PS} = 3.76 \times 10^{-3} \gg C^*$ g/mL, the Stokes–Einstein relation for the slow mode breaks down and the contribution for the high-frequency components increases. It is interesting to note that the polymer volume occupies only $\sim$0.5% of space in the present study.

In conclusion, we reemphasize our observation of a nonexponential behavior for $g^{(1)}(K,\tau)$ of the PMMA probe ($C_{PMMA} \ll C_{PMMA}^*$) in the isorefractive PS matrix over a range of PS concentrations ($C_{PS} > C_{PS}^*$) with PMMA size greater than the PS correlation length ($L_{PS} < R_{g,PMMA}$) whereas $g^{(1)}(K,\tau)$ of the same PMMA probe in the same mixed solvent, but without the semidilute PS coils, over the same KR_g range ($KR_g \sim 1$) exhibits a narrow characteristic line-width distribution $G(\Gamma)$ reflecting only the polydispersity of the PMMA probe. On the basis of the CONTIN method of data analysis, the nonexponential time correlation function $g^{(1)}(K,\tau)$ at relatively small scattering angles ($KR_{g,PMMA} \sim 1$ and $KL < 1$) where internal motions could not be observed appreciably by dynamic light scattering displayed a distinct high-frequency peak in $G(\Gamma)$, in addition to the low-frequency peak which can be identified with the translational motion of the PMMA probe. Numasawa, Hamada, and Nose[28] reported that for smaller PS probes in a semidilute solution of isorefractive PMMA in benzene $g^{(1)}(K,\tau)$ also exhibits a nonexponential decay at $KR_{g,PS} < 1$. Thus, the dynamical behavior of single probe chains in a semidilute solution of an isorefractive nonidentical polymer is more complex than originally anticipated. A great deal of caution needs to be exercised in identifying $\bar{\Gamma}$ with self-diffusion of the polymer probe. Results without due consideration on the origin of the nonexponential decay could deviate from correct answers in subtle ways. For our quarternary system, we have been able to identify the slow peak in $G(\Gamma)$ at $KR_{g,PMMA}$

$\tilde{<} 1$ with translational motions of the PMMA probe. At $C_{PS} \sim C_{PS}^*$, the translational diffusion coefficient still seems to obey the Stokes–Einstein relation. At higher PS concentrations, the translational characteristics of the slow peak begin to emphasize toward reptation. However, we have not been able to reach definitively an asymptotic region where the scaling relation $D_s \sim M^{-2}$ can be tested properly. Similarly, the bimodal behavior in $G(\Gamma)$ suggests that $\bar{\Gamma}$ values are susceptible to the instrumental bandwidth limitation. If the two modes are very far apart, we may be able to examine the dynamic behavior of each mode individually. With neglect of the high-frequency peak, distortion of $\bar{\Gamma}$ of the slow peak could become appreciable as the characteristic frequencies of the two modes become closer. Finally, polydispersity must necessarily play a very important role in broadening the overlap concentrations of the polymer matrix. Our dynamic measurements of PS semidilute solutions showed that single-exponential decay in $g^{(1)}(K,\tau)$ at $KL < 1$ for the cooperative diffusion coefficient could not be achieved until $C_{PS} \gg C_{PS}^*$. Thus, experimentally it is quite difficult to reach the asymptotic behavior often associated with polymer melts.

Acknowledgment. We gratefully acknowledge support of this work by the National Science Foundation Polymers Program (DMR 8314193) and the U.S. Army Research Office (DAAG2985K0067). Q.-M. Liang helped in sample preparation and performed some of the viscosity and refractive index measurements.

References and Notes

(1) Chu, B.; Nose, T. *Macromolecules* **1980**, *13*, 122.
(2) For example, see: Amis, E. J.; Han, C. C. *Polymer* **1982**, *23*, 1403.
(3) Chu, B. *Polym. J. (Tokyo)* **1985**, *17*(1), 225.
(4) Tirrell, M. *Rubber Chem. Technol.* **1984**, *57*, 523.
(5) Balloge, S.; Tirrell, M. *Macromolecules* **1985**, *18*, 819.
(6) Wesson, J. A.; Noh, I.; Kitano, T.; Yu, H. *Macromolecules* **1984**, *17*, 782.
(7) Eisele, M.; Burchard, W. *Macromolecules* **1984**, *17*, 1636.
(8) Brown, W. *Macromolecules* **1984**, *17*, 66.
(9) Hanley, B.; Balloge, S.; Tirrell, M. *Chem. Eng. Commun.* **1983**, *24*, 93.
(10) Lodge, T. P. *Macromolecules* **1983**, *16*, 1393.
(11) Martin, J. E. *Macromolecules* **1984**, *17*, 1279.
(12) Lin, C.-Y.; Rosen, S. L. *J. Polym. Sci.* **1982**, *20*, 1497.
(13) Lin, T.; Phillies, G. D. J. *J. Colloid Interface Sci.* **1984**, *100*, 82; Phillies, G. D. J.; Ullmann, G. S.; Ullmann, K.; Lin, T. *J. Chem. Phys.* **1985**, *82*(11), 5242.
(14) Phillies, G. D. J. *Macromolecules* **1986**, *19*, 2367.
(15) Strazielle, C. *Light Scattering from Polymer Solutions*; Huglin, M. B., Ed.; Academic: London and New York, 1972.
(16) Chu, B.; Lee, D. C. *Macromolecules* **1984**, *17*, 926.
(17) de Gennes, P.-G. *Macromolecules* **1976**, *9*, 587.
(18) Chu, B.; Ford, J. In *Proceedings of the 5th International Conference on Photon Correlation Techniques in Fluid Mechanics*; Schulz-DuBois, E. O., Ed.; Springer-Verlag: New York, 1983.
(19) Provencher, S. W. *Computer Physics Commun.* **1972**, *27*, 229.
(20) Koppel, D. E. *J. Chem. Phys.* **1972**, *57*, 4814.
(21) Chu, B.; Onclin, M.; Ford, J. R. *J. Phys. Chem.* **1984**, *88*, 6566.
(22) Adam, M.; Delsanti, M. *Macromolecules* **1977**, *10*, 1229.
(23) Lin, Y.-H. *Macromolecules* **1984**, *17*, 2846.
(24) Ronca, G. *J. Chem. Phys.* **1983**, *79*(2), 1031.
(25) Stockmayer, W. H.; Schmidt, M. *Pure Appl. Chem.* **1982**, *54*, 407.
(26) Kuhn, R.; Cantow, H.-J.; Burchard, W. *Angew. Makromol. Chem.* **1968**, *2*, 146, 157. Kuhn, R.; Cantow, H.-J. *Makromol. Chem.* **1969**, *122*, 65.
(27) Lodge, T. P.; Wheeler, L. M.; Hanley, B.; Tirrell, M. *Polym. Bull. (Berlin)* **1986**, *15*, 35.
(28) Numasawa, M.; Hamada, T.; Nose, T. *J. Polym. Sci., Polym. Phys. Ed.* **1986**, *24*, 19.
(29) Kops-Werkhoven, M. M.; Fijnaut, A. M. *J. Chem. Phys.* **1982**, *77*, 2242.
(30) Pusey, P. N.; Tough, R. J. A. In *Dynamic Light Scattering*; Pecora, R., Ed.; Plenum: New York, 1985.
(31) Phillies, G. D. J. *J. Chem. Phys.* **1983**, *79*, 2325.
(32) Pusey, P. N.; Fijnaut, H. M.; Vrij, A. *J. Chem. Phys.* **1982**, *77*, 4270.
(33) See also: Chu, B.; Wu, D.-Q.; Liang, G.-M. *Macromolecules* **1986**, *19*, 2665.

Hydrodynamic Properties of Short Poly(dimethylsiloxane) Chains. Numerical Results and Comparison with Experimental Data

Ana M. Rubio

Departamento de Quimica General y Macromolêculas, Facultad de Ciencias, Universidad Nacional de Educaciôn a Distancia (U.N.E.D.), 28040 Madrid, Spain

Juan J. Freire*

Departamento de Quimica Fisica, Facultad de Ciencias Quimicas, Universidad Complutense, 28040 Madrid, Spain

José Garcia de la Torre

Departamento de Quimica Fisica, Facultad de Ciencias Quimicas y Matemâticas, Universidad de Murcia, 30001 Murcia, Spain. *Received October 27, 1986*

ABSTRACT: Numerical results for the friction coefficient and the viscosity of short poly(dimethylsiloxane) molecules in solution have been obtained by using preaveraged or approximate formulas and also employing a simulation method that avoids preaveraging. The latter method together with the choice of chain-length-dependent radii for the frictional units yields results in excellent agreement with experimental data for translation. The comparison between our results and experimental data is only fair in the case of viscosity maybe because of the introduction of an approximate procedure to eliminate solvent effects. As a difference with respect to our previous study of less flexible *n*-alkanes, our numerical values corresponding to chains with the highest number of repeating units for which the calculations are flexible are already very close to the long-chain limits. Therefore, our work covers the range of molecular weights going from the oligomeric to the polymeric (Gaussian) behavior.

Introduction

The theoretical interpretation of the hydrodynamic properties of relatively short-chain molecules like *n*-alkanes or oligomers of poly(dimethylsiloxane) (PDMS) can only be performed through the use of realistic molecular models. These models should take into account the varying permeability to the solvent flow of chains with a different number of frictional units. An appropriate procedure

0024-9297/87/2220-1619$01.50/0